Journal of the Optical Society of America A
OPTICS, IMAGE SCIENCE, AND VISION

Analytic plenoptic camera diffraction model and radial distortion analysis due to vignetting

M. Ardebili[1,*] and G. Saavedra[2]

[1]Christian-Albrechts-Universität zu Kiel, 24118 Kiel, Germany
[2]3D Imaging & Display Laboratory, Universitat de València, E46100 Burjassot, Spain
*daniard@gmail.com

Received 20 January 2023; revised 8 May 2023; accepted 16 May 2023; posted 16 May 2023; published 28 June 2023

Using a mathematical approach, this paper presents a generalization of semi-analytical expressions for the point spread function (PSF) of plenoptic cameras. The model is applicable in the standard regime of the scalar diffraction theory while the extension to arbitrary main lens transmission functions generalizes a priori formalism. The accuracy and applicability of the model is well verified against the exact Rayleigh–Sommerfeld diffraction integral and a rigorous proof of convergence for the PSF series expression is made. Since vignetting can never be fully eliminated, it is critical to inspect the image degradation it poses through distortions. For what we believe is the first time, diffractive distortions in the diffraction-limited plenoptic camera are closely examined and demonstrated to exceed those that would otherwise be estimated by a geometrical optics formalism, further justifying the necessity of an approach based on wave optics. Microlenses subject to the edge diffraction effects of the main lens vignetting are shown to translate into radial distortions of increasing severity and instability with defocus. The distortions due to vignetting are found to be typically bound by the radius of the geometrical defocus in the image plane, while objects confined to the depth of field give rise to merely subpixel distortions.

https://doi.org/10.1364/JOSAA.485284

1. INTRODUCTION

A wave optics generic model for the light field point spread function (LF-PSF) is substantially advantageous for plenoptic cameras. This model provides the tools for a quantitative quality assessment of these imaging systems in the presence of aberrations and diffraction. An accurate model of the LF-PSF provides direct insight into the camera's optical influence on depth estimation algorithms. From here, one can modify the intrinsic parameters of the plenoptic camera to optimize its optical design.

Recent research in light field technology has been aimed at improving the overall resolution performance of these imaging systems. In [1], a scheme was devised to enhance the effective refocus resolution at the expense of the angular resolution by displacing the microlens array (MLA) to a different distance from the sensor. Currently, the presence of multiple microlens types allows an enhanced depth of field in a Raytrix camera [2]. Alternatively, an extended depth of field for enhanced depth resolution can be achieved by compensating for the out-of-focus blur through selective depth deconvolution [3]. A design for ultimate 3D microscopy was proposed by placing the MLA at the aperture stop of the microscope objective. The net result is an extended depth of field by 2.75-fold and a lateral resolution increase of $\sqrt{2}$ multiplied the spatial resolution of regular integral microscopy [4]. Further research was conducted to discover the real resolution limit in integral microscopy and to optically acquire perspective images with unprecedented resolution [5]. Post-processing methods are also used to achieve enhanced resolution. In the inspection of fluorescent samples, sensor noise and sensitivity is problematic and large pixels are necessary to handle low-light conditions that cause undersampling issues. By analyzing sampling patterns, the extent to which computational super-resolution can be achieved for resolution enhancement was explored in [6].

Lytro Inc. founder Ng [7] conceived the Fourier slice photography theorem to devise a Fourier-domain algorithm for digital refocusing. It is done by stripping the suitable 2D Fourier slice of the light field's Fourier transform, with a successive inverse Fourier transform of the result. A two-step algorithm was proposed through an initial reconstruction of the scene depth by determining the correspondence between views. From this, a model for the spatially variant PSF was obtained in a Bayesian deconvolution scheme to estimate the superresolved image with an extended depth of field [8]. Through ray tracing methods and the use of ray space diagrams in [9], aberrated rays were digitally reallocated to their ideal image points to synthesize light field photographs with reduced lens aberrations. More recently, a full simulation of the plenoptic camera in Blender was devised to synthesize light field images of elaborate scenes using accurate finite ray tracing that accounts for the complete optical design of the main lens and MLA [10]. However, none of these

1084-7529/23/071451-17 Journal

approaches explicitly use wave optics to explain diffraction in the image formation process.

It should be strongly emphasized that neither spot diagrams nor ray intersection patterns accurately represent the genuine irradiance variation in the image plane and a fully diffraction-based computation is necessary [11]. In particular, wave optics quantitively describes the effects of the vignetting with superior accuracy over geometrical optics. As shown in Section 5, the explanatory scope of a geometrical optics model does not sufficiently estimate the complex distortions predicted by this diffraction model. Moreover, a realistic and accurate model for the LF-PSF offers the prospect of image restoration of the microimages by deconvolution and super-resolution techniques, which will improve the depth resolution and image contrast [12]. Improvement in the image quality by such methods is constrained by both the accuracy of the diffraction model and the optical resolution versus the sensor resolution. Therefore, deconvolution is most advantageous when applied to microscopy where the system's impulse response is observably greatest.

In the pursuit of a generic wave optics model that assimilates aberrations, it is also important to acknowledge the inevitable degradation of image quality that would occur as a result of such wavefront deformations. As shown in [13], using the Cauchy–Schwarz inequality, image contrast can never increase as a result of aberrations and will in general decrease the contrast. Furthermore, severe aberrations can limit the effective cutoff frequency, while within certain frequency bands, aberrations can cause the optical transfer function (OTF) to become negative or complex valued, which gives rise to contrast reversal where intensity maxima vanish and vice versa [13].

Nonetheless, the effect of aberrations on image quality specifically in the plenoptic camera has only been more recently investigated. More generally, in the presence of aberrations, the set of phase aberrations for a given microlens, depends on its lateral coordinates in the MLA plane due the variation in field angle it subtends with respect to the main lens exit pupil. Decentered microlenses have nodes in the field-dependent Zernike coefficients that approximate the wavefront aberration function. Interestingly, even the main lens on axis aberrations such as spherical aberrations will not uniquely cascade to spherical aberrations in the microlenses. This is due to the fact that decentered microlenses with respect to the main lens optical axis depart from circular symmetry. The severity of the arising off-axis aberrations has been studied in detail [14]. It has been shown that for an aberration-free system composed of circular apertures under arbitrary wavefront tilting when the Fresnel diffraction integral holds, can only give rise to radial distortions in the microimages [15]. It may be claimed that radial distortions can strictly occur for an axially focusing rotationally symmetric (potentially aberrated) wavefront from the main lens exit pupil, even under the exact Rayleigh–Sommerfeld integral regardless of the final emergent wavefront at the microlens exit pupils. The alternate case is for a tilted paraxial aberration-free wavefront, where the Fresnel approximation applies to diffraction from the microlenses. The problem of microimage distortions along with solutions to compensate for them is a relatively new study. Distortions due to surface defects in the microlenses have been investigated [16].

Based on the prior research discussed in the literature review above, this paper proposes what we believe, to the best of our knowledge, is a novel model based on wave optics that extends the conditions of applicability of a former model [17]. The solution presented here demonstrates and advocates the notion that realistic and accurate computations of the LF-PSF in the spatial domain is achievable for the desirable end goals outlined above. To the best of our knowledge, this mathematical approach is entirely original and state of the art in the area of light field photography. It generalizes the approach in [17] to general pupil locations in the presence of arbitrary wavefront tilting and transmission functions for the main lens. For practicality, however, it shall be assumed that the microlenses are not subject to any main lens aberrations. Otherwise, any invariance properties of the LF-PSF will be violated, introducing an impractical level of complexity to computational schemes. In this way, the analysis may be restricted to the aberration-free case in the presence of inherent vignetting within the system.

Despite these assumptions, in a number of respects this model supersedes other approaches such as the aberration-free plenoptic camera with a thin lens main lens and microlenses proposed in [18]. This model introduces unnecessary restrictions and complexity to the image formation. In particular, the intermediate image is assumed to form prior to the MLA and is thus not valid for defocusing in the Galilean configuration. The excessive number of highly oscillatory integrals that have to be numerically computed just to simulate the impulse response is also computationally inefficient. In [3], the LF-PSF is assumed to be spatially transversally invariant and isotropic, as the vignetting induced by the finite aperture of the main lens is not accounted for. In [12], the diffraction is modeled for the light field microscope to perform deconvolution to enhance the spatial resolution of the samples; in [19,20], plenoptic 1.0 setups are considered where microlenses are placed in the back focal plane of the main lens and with the MLA to sensor distance fixed to the microlens focal length. This assumption is extended for the case of arbitrary distances.

Another powerful application of knowledge of the LF-PSF is that it allows for a high accuracy assessment of distortions through computations of the centroids of the intensity response. Such computations are necessary as experimental data suggests an inadequacy in the geometrical optics models typically used in the metric calibration of plenoptic cameras. For example, the common pinhole model for the microlenses cannot explain the sheared curvilinear epipolar geometry on the local scale of the microimages that is experimentally observed when imaging a rectilinear target at a fixed depth plane. Although this is a likely complication of multiple phenomena, distortions must be at least partly attributed to wavefront aberrations and inevitable vignetting inherent within the system. To investigate the claim of the latter, succeeding the formulation of this model, radial distortions are shown to increase in severity with both the coupled main lens vignetting and defocus at the sensor plane. For the first time in the literature of light field photography, this is quantitatively analyzed and discussed in depth as accomplished in Section 5 of this paper. This is the first step to comprehend and estimate noise in the reconstructed depth map of a light field camera, forming the basis of any schematic procedure required to rectify or minimize these systematic errors in the camera's calibration, which is a reason for a model that attests to these observations, as presented here in this paper.

2. THEORY

In this section, a generic expression for the LF-PSF is derived from first principles. By using the results of the extended Nijboer–Zernike (ENZ) theory [21–25], analytical expressions for the microlens pupil light amplitude distributions are obtained. Through considerations of symmetry and by exploiting the use of an unconventional shifted coordinate frame centered on the chief ray intersection with the microlens exit pupil, integration is handled by expressing the LF-PSF as an infinite series of Hankel transforms.

Note that in the following sections, all bold quantities refer to 2D position vectors that lie in planes perpendicular to the optical axis. For simplicity of notation, whenever reference to a function $F(x, y)$ of variables x, y is made, in a distinct coordinate frame, $F(u, v)$ represents the re-expression of $F(x, y)$ in terms of the variables u, v, while in general, $F(x, y) \neq F(u, v)$.

Assume the situation depicted in Fig. 1, where a considered object point $\mathscr{P}$ is located at a transverse position described by the vector $\boldsymbol{X}_o$ and a distance p_o from the entrance pupil plane of the main lens of a light field imaging system.

A particular microlens is located with its entrance pupil plane at a distance a from the exit pupil of the main lens, with its optical axis displaced parallel by $\widetilde{\boldsymbol{c}}_\ell$ with respect to the optical axis of the main lens. Finally, the sensor plane lays on a transverse plane at a distance b from the exit pupil of the microlens. The main lens intermediate image forms at $\mathscr{P}'$ while the final microlens image forms at $\mathscr{P}'_\ell$.

From now on, the very usual case of a well-corrected main lens is assumed, generating negligible field and point aberration. The information regarding the wavefront tilting and defocus is encapsulated in the field distribution incident on the microlens array from the main lens. Under this hypothesis, the amplitude PSF (APSF) in the presence of wavefront tilting arriving to the microlens's entrance pupil may be expressed as

$$U^-(\boldsymbol{\xi}) = e^{i\frac{k}{a}(\widetilde{\boldsymbol{c}}_o - \boldsymbol{c}_e)\cdot\boldsymbol{\xi}}\, U\left(\boldsymbol{\xi} - \widetilde{\boldsymbol{c}}_o, a;\, p_o\right), \tag{1}$$

where $U(\boldsymbol{\xi}, a;\, p_o)$ stands for the axial APSF of the main lens at lateral position $\boldsymbol{\xi}$ (as measured from the main lens' optical axis) and at distance a from its exit pupil plane, for the object depth p_o, and $k = \frac{2\pi}{\lambda}$ is the wavenumber for wavelength λ. Here, $\widetilde{\boldsymbol{c}}_o$ stands for the lateral position vector of the intersection of the main lens' chief ray with the microlens' entrance pupil, as measured from the main lens's optical axis, and $\boldsymbol{c}_e$ represents the position vector of the main lens exit pupil center. From now on, it is appropriate to express this response relative to the microlens optical axis. Thus, by using the new lateral coordinate $\boldsymbol{x} = \boldsymbol{\xi} - \widetilde{\boldsymbol{c}}_\ell$, neglecting constant phase terms, the scalar field amplitude arriving at the entrance pupil of the microlens is

$$U_\ell^-(\boldsymbol{x}) = e^{i\frac{k}{a}(\boldsymbol{\delta}_\ell^- + \widetilde{\boldsymbol{c}}_\ell - \boldsymbol{c}_e)\cdot\boldsymbol{x}}\, U\left(\boldsymbol{x} - \boldsymbol{\delta}_\ell^-, a;\, p_o\right), \tag{2}$$

where $\boldsymbol{\delta}_\ell^- = \widetilde{\boldsymbol{c}}_o - \widetilde{\boldsymbol{c}}_\ell$ is the lateral position vector of the chief ray intersection with the microlens' entrance pupil, as measured from its optical axis. The microlens amplitude transmittance from its entrance to its exit pupil is then given by

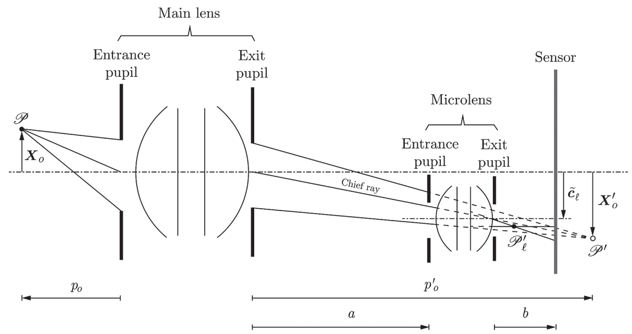

Fig. 1. Depiction of a general model for the main lens and a single microlens. Note that for the sake of clarity it is assumed that the microlens optical axis is contained in the plane defined by the object point $\mathscr{P}$ and the optical axis of the main lens. In a more general situation, the position vector $\widetilde{\boldsymbol{c}}_\ell$ might not be on the figure plane, and the center of the main lens exit pupil $\boldsymbol{c}_e$ may not lie on the main lens optical axis.

$$t_{n_\ell}(\boldsymbol{x}) = e^{-i\frac{k}{2f_{n_\ell}}|\boldsymbol{x}|^2}\, P_{n_\ell}(\boldsymbol{x}), \tag{3}$$

where $P_{n_\ell}(\boldsymbol{x})$ is the pupil function of the microlens, f_{n_ℓ} is the distance from its exit pupil to its image focal plane and n_ℓ is the assigned index-generating function that ascribes the microlens type to a given ℓ-th microlens. Note that an extra magnification factor M_p must be considered in this step, accounting for the scaling between the entrance and exit pupil conjugated planes. In this way, the amplitude distribution emerging from the microlens' exit pupil is given by

$$U_\ell^+(\boldsymbol{x}) = e^{-i\frac{k}{2f_{n_\ell}}|\boldsymbol{x}|^2}\, U\left(\frac{\boldsymbol{x} - \boldsymbol{\delta}_\ell}{M_p}, a;\, p_o\right) P_{n_\ell}(\boldsymbol{x}) e^{i\frac{k}{M_p a}\left(\frac{\boldsymbol{\delta}_\ell}{M_p} + \widetilde{\boldsymbol{c}}_\ell - \boldsymbol{c}_e\right)\cdot\boldsymbol{x}}, \tag{4}$$

$\boldsymbol{\delta}_\ell = M_p \boldsymbol{\delta}_\ell^-$ being the transverse vector coordinate of the exiting location of the chief ray (as measured from the microlens optical axis).

We shall adopt the Fresnel integral with a defocus term for diffraction from the microlenses because it enables analytical treatment with greater ease. Given the lateral coordinates $\boldsymbol{x}_\ell = \boldsymbol{x}^s - \widetilde{\boldsymbol{c}}_\ell$, the Fresnel integral takes the form

$$U_\ell^s(\boldsymbol{x}_\ell) = \iint_{\mathbb{R}^2} e^{i\frac{k}{2b}|\boldsymbol{x}|^2}\, U_\ell^+(\boldsymbol{x}) e^{-i\frac{k}{b}\boldsymbol{x}_\ell\cdot\boldsymbol{x}}\, \mathrm{d}^2\boldsymbol{x}. \tag{5}$$

The substitution of Eq. (4) into Eq. (5) then gives

$$U_\ell^s(\boldsymbol{x}_\ell) = \iint_{\mathbb{R}^2} e^{i\alpha_{n_\ell}|\boldsymbol{x}|^2}\, U\left(\frac{\boldsymbol{x} - \boldsymbol{\delta}_\ell}{M_p}, a;\, p_o\right) P_{n_\ell}(\boldsymbol{x}) e^{-i\frac{k}{b}\left[\boldsymbol{x}_\ell - \frac{b}{M_p a}\left(\frac{\boldsymbol{\delta}_\ell}{M_p} + \widetilde{\boldsymbol{c}}_\ell - \boldsymbol{c}_e\right)\right]\cdot\boldsymbol{x}}\, \mathrm{d}^2\boldsymbol{x}, \tag{6}$$

where $\alpha_{n_\ell} = \frac{k}{2}\left(\frac{1}{b} - \frac{1}{f_{n_\ell}}\right)$. By defining the microimage center as the LF-PSF's centroid for when $\boldsymbol{\delta}_\ell = 0$, it follows that the vector quantity $\boldsymbol{\Delta}_\ell = \frac{b}{M_p a}(\widetilde{\boldsymbol{c}}_\ell - \boldsymbol{c}_e)$ is the lateral coordinate offset of the ℓ-th microlens center to its microimage center $\boldsymbol{c}'_\ell$. It is now ideal to express the integration position $\boldsymbol{x}$ in Eq. (6) in relation to the intersection of the main lens' chief ray with the microlens'

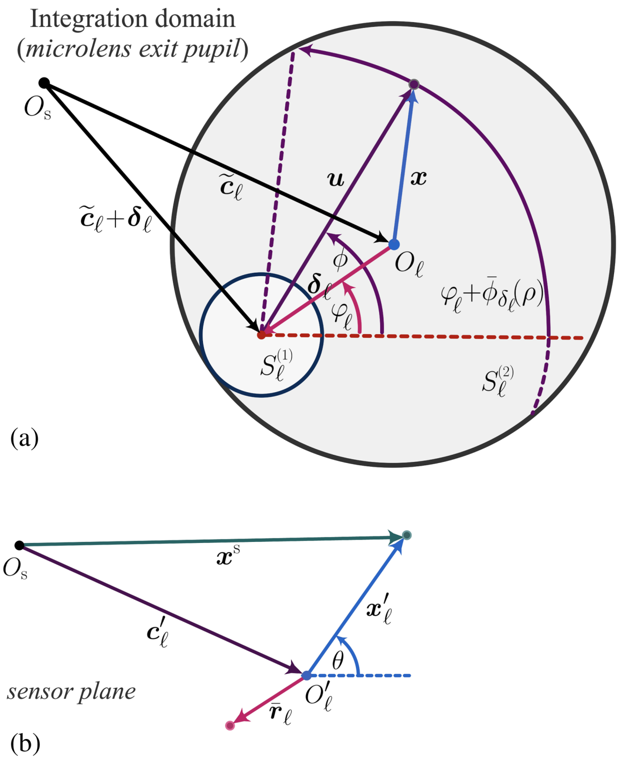

Fig. 2. Geometry used in the computation of the APSF onto the sensor plane. The main lens' optical axis runs perpendicular to the figure plane passing through the black spot at O_s, while the microlens' optical axis intersects the figure plane in the blue spot at O_ℓ, as shown in (a). The pink points represents the chief ray impact point onto the microlens' exit pupil and the sensor planes as shown, respectively, in (a) and (b).

exit pupil, by using the coordinate $\boldsymbol{u}=\boldsymbol{x}-\boldsymbol{\delta}_\ell$. Introducing the additional coordinate shift $\boldsymbol{x}'_\ell=\boldsymbol{x}_\ell-\boldsymbol{\Delta}_\ell$, it is straightforward to obtain (see Fig. 2)

$$\begin{aligned}U_\ell^s(\boldsymbol{x}'_\ell)\propto&\iint_{\mathbb{R}^2}e^{i\alpha_{n_\ell}|\boldsymbol{u}|^2}U\left(\frac{\boldsymbol{u}}{M_p},a;\,p_o\right)\\&P_{n_\ell}(\boldsymbol{u}+\boldsymbol{\delta}_\ell)e^{-i\frac{k}{b}(\boldsymbol{x}'_\ell-\bar{\boldsymbol{r}}_\ell)\cdot\boldsymbol{u}}\,\mathrm{d}^2\boldsymbol{u}\\\propto&\,\mathcal{F}\left\{e^{i\alpha_{n_\ell}|\boldsymbol{u}|^2}U\left(\frac{\boldsymbol{u}}{M_p},a;\,p_o\right)P_{n_\ell}(\boldsymbol{u}+\boldsymbol{\delta}_\ell);\,\frac{\boldsymbol{x}'_\ell-\bar{\boldsymbol{r}}_\ell}{\lambda b}\right\},\end{aligned}\tag{7}$$

where the vector

$$\bar{\boldsymbol{r}}_\ell=b\left(\frac{1}{M_p^2a}+\frac{1}{b}-\frac{1}{f_{n_\ell}}\right)\boldsymbol{\delta}_\ell\tag{8}$$

can be shown to be the position vector (as measured from the microimage center) of the intersection point of the chief ray onto the sensor plane, while $\mathcal{F}\{f(\boldsymbol{t});\,\boldsymbol{v}\}$ stands for the 2D Fourier transformation of the function $f(\boldsymbol{t})$ at spatial frequency $\boldsymbol{v}$.

For the purpose of this work, it is very convenient to use polar coordinates in Eq. (7), both in the integration domain and the sensor plane. Thus, we introduce the polar coordinates (ρ,ϕ), where $\rho=|\boldsymbol{u}|$, $\phi=\arg\{\boldsymbol{u}\}$ in the integration domain (centered on the intersection point of the chief ray and the microlens' exit pupil plane). Furthermore, in the sensor plane, we have polar coordinates (r,θ), where $r=|\boldsymbol{x}'_\ell|$, $\theta=\arg\{\boldsymbol{x}'_\ell\}$, (with the center of the microimage $\boldsymbol{c}'_\ell$ as reference), as shown in Fig. 2. These changes lead to

$$\begin{aligned}U_\ell^s(r,\theta)\propto&\int_0^{2\pi}\int_0^\infty e^{i\alpha_{n_\ell}\rho^2}U\left(\frac{\rho}{M_p},\phi,a;\,p_o\right)\\&P_{n_\ell}(\varrho(\rho,\phi),\vartheta(\rho,\phi))\\&e^{i\gamma_o(r,\theta)\rho\cos(\phi+\varphi_o(r,\theta))}\rho\,\mathrm{d}\rho\,\mathrm{d}\phi,\end{aligned}\tag{9}$$

where

$$\begin{aligned}&\gamma_o(r,\theta)=\frac{k}{b}|\bar{\boldsymbol{r}}_\ell-\boldsymbol{x}'_\ell|,\qquad\varrho(\rho,\phi)=|\boldsymbol{u}+\boldsymbol{\delta}_\ell|,\\&\varphi_o(r,\theta)=-\arg\left\{\bar{\boldsymbol{r}}_\ell-\boldsymbol{x}'_\ell\right\},\qquad\vartheta(\rho,\phi)=\arg\{\boldsymbol{u}+\boldsymbol{\delta}_\ell\}.\end{aligned}\tag{10}$$

If P_{n_ℓ} is a uniform circular aperture, from [26] we may take $P_{n_\ell}(\boldsymbol{x})=1$, $|\boldsymbol{x}|\le r_e$ and $P_{n_\ell}(\boldsymbol{x})=0$, $|\boldsymbol{x}|>r_e$, where r_e is the radius of the microlens exit pupil; therefore, in the polar coordinates (ρ,ϕ), the domain of integration can be represented by the disjoint union of sets $S_\ell:=S_\ell^{(1)}\cup S_\ell^{(2)}$, where

$$\bar{\phi}_{\delta_\ell}(\rho)=\mathrm{Re}\big[\arccos(\zeta_{\delta_\ell}(\rho))\big],\qquad\zeta_{\delta_\ell}(\rho)=\frac{\delta_\ell^2-r_e^2+\rho^2}{2\delta_\ell\rho},\tag{11}$$

for $\delta_\ell=|\boldsymbol{\delta}_\ell|$.

Therefore, the pupil function is now $P_{n_\ell}(\rho,\phi)=1$ for $(\rho,\phi)\in S_\ell$ and $P_{n_\ell}(\rho,\phi)=0$ for $(\rho,\phi)\notin S_\ell$; hence,

$$\begin{aligned}S_\ell^{(1)}&=\begin{cases}(\rho,\phi)\in\mathbb{R}_{\ge0}\times[0,2\pi):\ \rho\in[0,\max\{r_e-\delta_\ell,0\}],\\\qquad\qquad\qquad\qquad\phi\in[0,2\pi),\ \delta_\ell\in[0,r_e)\\\varnothing,\ \delta_\ell\in(r_e,\infty)\end{cases}\\S_\ell^{(2)}&=\begin{cases}(\rho,\phi)\in\mathbb{R}_{\ge0}\times[0,2\pi):\ \rho\in(|r_e-\delta_\ell|,r_e+\delta_\ell),\\\qquad\qquad\qquad\qquad|\phi-\varphi_\ell|<\bar{\phi}_{\delta_\ell}(\rho),\ \delta_\ell\in(0,\infty)\\\varnothing,\ \delta_\ell=0\end{cases}\end{aligned}\tag{12}$$

where $\varphi_\ell=-\arg\{\boldsymbol{\delta}_\ell\}$.

From the geometry of intersecting circles [27], the limits of integration are given by the relations (see Fig. 2)

$$\begin{aligned}&\phi_0(\rho)=\varphi_\ell-\bar{\phi}_{\delta_\ell}(\rho),\qquad\rho\in[0,\infty)\qquad\rho_0=0,\\&\phi_1(\rho)=\varphi_\ell+\bar{\phi}_{\delta_\ell}(\rho),\qquad\rho\in[0,\infty)\qquad\rho_1=r_e+\delta_\ell,\ \delta_\ell\ge0.\end{aligned}\tag{13}$$

Finally, we obtain

$$\begin{aligned}U_\ell^s(r,\theta)=&\int_{\rho_0}^{\rho_1}\rho e^{i\alpha_{n_\ell}\rho^2}\int_{\phi_0(\rho)}^{\phi_1(\rho)}U\left(\frac{\rho}{M_p},\phi,a;\,p_o\right)\\&e^{i\gamma_o(r,\theta)\rho\cos(\phi+\varphi_o(r,\theta))}\mathrm{d}\phi\,\mathrm{d}\rho.\end{aligned}\tag{14}$$

It is clear in Fig. 3 that the plots of $\bar{\phi}_{\delta_\ell}(\rho)$ directly correspond to the set of points over which one must integrate over the aperture in the polar coordinate frame (ρ,ϕ). For radial

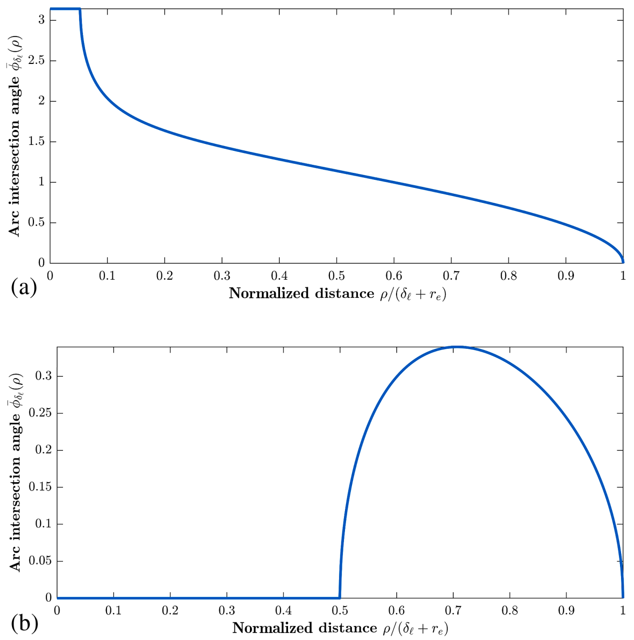

Fig. 3. Exemplary plots of the $\bar{\phi}_{\delta_\ell}(\rho)$ function on the domain $\rho \in (0, r_e + \delta_\ell)$ for cases $\delta_\ell \le r_e$: (a) showing $\bar{\phi}_{\delta_\ell}(\rho) = \pi$ on $\rho \in [0, r_e - \delta_\ell)$, and (b) $\delta_\ell > r_e$ with $\bar{\phi}_{\delta_\ell}(\rho) = 0$ on $\rho \in [0, \delta_\ell - r_e)$.

values $\rho \in [0, \max\{0, r_e - \delta_\ell\}\}$, the integration is on a full circle within the microlens aperture, so $\bar{\phi}_{\delta_\ell}(\rho) = \pi$ on this domain; whereas on the intervals $\rho \in [|r_e - \delta_\ell|, r_e + \delta_\ell]$ and $\rho \in [0, \max(\delta_\ell - r_e)) \cup [r_e + \delta_\ell, \infty)$, $\bar{\phi}_{\delta_\ell}(\rho) \in [0, \pi]$. Using solutions to the ENZ theory for a main lens obeying the Debye diffraction integral, the exit pupil distributions may be expressed completely analytically for a general defocus. Hence, we are left to calculate diffraction from the microlens exit pupils to the sensor to acquire the final LF-PSFs of the plenoptic camera.

A. Generalization to Arbitrary Main Lens Transmission Functions

To use the analytical results from ENZ theory applied to the main lens response onto the microlens' entrance pupil $U(\frac{\rho}{M_p}, \phi, a;\ p_o)$ [21–25], we first decompose the main lens' generalized pupil function in terms of the Zernike polynomials, $Z_p^q(\upsilon, \omega) = R_p^q(\upsilon)\cos[q\omega - (1 - |q|/q)\pi/4]$; namely,

$$P(\upsilon, \omega) = \sum_{p,q} \beta_p^q Z_p^q(\upsilon, \omega), \quad p \in \mathbb{N},\ q \in \mathbb{Z} : p - |q| \ge 0 \text{ even}, \tag{15}$$

with (υ, ω) being the polar coordinates onto the main lens exit pupil, normalized to this aperture radius. The complex valued β_p^q coefficients in the Zernike expansion can be determined using either inner products or the least squares method [21]. Propagating the field given by Eq. (15) onto the microlens' entrance pupil using the Debye approximation, ENZ framework predicts

$$U(\rho, \phi, a;\ p_0) = 2\sum_{p,q} i^{|q|}\beta_p^q V_p^q(\rho')e^{iq\phi}, \tag{16}$$

for normalized radial coordinate $\rho' = \mathrm{NA}'\rho/\lambda$, where NA' stands for the numerical aperture of the main lens on the image side. The functions used in this decompositions are defined as

$$V_p^q(\rho') = \int_0^1 e^{if\upsilon^2} R_p^q(\upsilon) J_q(2\pi\rho'\upsilon)\upsilon \mathrm{d}\upsilon \tag{17}$$

and have analytical solutions in the form of an infinite series as provided by the ENZ theory, and J_s are the Bessel functions of the first kind, while the defocus coefficient is defined as

$$f = -2\pi\frac{a - p_0'}{\lambda}\left(1 - \sqrt{1 - \mathrm{NA}'^2}\right). \tag{18}$$

Note that to avoid a cumbersome notation, dependency on the defocus parameter of the functions $V_p^q(\rho')$ has been omitted.

Finally, by substituting Eq. (16) into Eq. (9), considering the Jacobi–Anger expansion

$$e^{i\gamma_o\rho\cos(\phi+\varphi_o)} = \sum_{s=-\infty}^{\infty} i^s J_s(\gamma_o\rho)e^{is(\phi+\varphi_o)}, \tag{19}$$

we finally obtain

$$\begin{aligned} U_\ell^s(r, \theta) &= \int_{\rho_0}^{\rho_1} \rho e^{i\alpha_{n_\ell}\rho^2} \int_{\phi_0(\rho)}^{\phi_1(\rho)} \left(\sum_{p,q} i^{|q|}\beta_p^q V_p^q\left(\frac{\rho'}{M_p}\right)e^{iq\phi}\right) \\ &\quad \left(\sum_{s=-\infty}^{\infty} i^s J_s(\gamma_o(r,\theta)\rho)e^{is(\phi+\varphi_o(r,\theta))}\right)\mathrm{d}\phi\mathrm{d}\rho \\ &= \sum_{p,q} i^{|q|}\beta_p^q \left(\sum_{s=-\infty}^{\infty} i^s e^{is\varphi_o(r,\theta)} \int_{\rho_0}^{\rho_1} V_p^q\left(\frac{\rho'}{M_p}\right)\right. \\ &\quad \left. e^{i\alpha_{n_\ell}\rho^2}\left(\int_{\phi_0(\rho)}^{\phi_1(\rho)} e^{i(s+q)\phi}\mathrm{d}\phi\right) J_s(\gamma_o(r,\theta)\rho)\rho\mathrm{d}\rho\right) \\ &= \sum_{p,q} i^{|q|}\beta_p^q \left(\sum_{s=-\infty}^{\infty} i^s e^{is\varphi_o(r,\theta)} \mathscr{I}_{ps}^q(r,\theta)\right), \end{aligned} \tag{20}$$

where

$$\mathscr{I}_{ps}^q(r,\theta) = \int_{\rho_0}^{\rho_1} V_p^q\left(\frac{\rho'}{M_p}\right) e^{i\alpha_{n_\ell}\rho^2}\left(\int_{\phi_0(\rho)}^{\phi_1(\rho)} e^{i(s+q)\phi}\mathrm{d}\phi\right) J_s(\gamma_o(r,\theta)\rho)\rho\mathrm{d}\rho. \tag{21}$$

The expression above was obtained having taken advantage of term-by-term integration of the infinite series, which is applicable due to legitimacy of Lebesgue's dominated convergence theorem. The theorem holds since, for any arbitrary number of terms, the partial sum defining the integrand is bounded above and converges pointwise to the limit function $U(\frac{\rho}{M_p}, \phi, a;\ p_o)e^{i\gamma_o(r,\theta)\rho\cos(\phi+\varphi_o(r,\theta))}$. For a proof, see Appendix A. Also since the ENZ theory and Jacobi–Anger expansion have allowed the integrand to be expressed as a sum of multiplicatively separable functions, the above integration above can be carried out much more easily. Using the definitions of $\phi_0(\rho)$ and $\phi_1(\rho)$, the straightforward angular integration of Euler's formula in the expression above now gives

$$\mathscr{I}^q_{ps}(r,\theta) = e^{i(s+q)\varphi_\ell} \int_0^\infty g_{s+q}(\rho) V^q_p\left(\frac{\rho'}{M_p}\right) e^{i\alpha_{n_\ell}\rho^2} J_s(\gamma_o(r,\theta)\rho)\rho\mathrm{d}\rho, \tag{22}$$

where $g_n(\rho) = 2\bar{\phi}_{\delta_\ell}(\rho)\mathrm{sinc}(n\bar{\phi}_{\delta_\ell}(\rho))$ for $n \in \mathbb{Z}$. One may alternatively express $g_n(\rho) = \frac{2}{n}(1-(\zeta_{\delta_\ell}(\rho))^2)^{1/2} U_{n-1}(\zeta_{\delta_\ell}(\rho))$, where U_n is the Chebyshev polynomial of the second kind of nth degree [28]. Finally, Eq. (22) may be expressed in the concise form

$$\mathscr{I}^q_{ps}(r,\theta) = e^{i(s+q)\varphi_\ell}\mathcal{H}_s\left\{u^q_{ps}(\rho);\, \gamma_o(r,\theta)\right\}, \tag{23}$$

for $u^q_{ps}(\rho) = g_{s+q}(\rho)V^q_p\left(\frac{\rho'}{M_p}\right)e^{i\alpha_{n_\ell}\rho^2}$, where the sth order Hankel transform of $v(\rho)$ is given by the equation $\mathcal{H}_s\{v(\rho);\gamma\} = \int_0^\infty v(\rho)J_s(\gamma\rho)\rho\mathrm{d}\rho$.

Note that the definition of $\bar{\phi}_{\delta_\ell}(\rho)$ and $\zeta_{\delta_\ell}(\rho)$ leads to a compact support for $g_n(\rho)$, vanishing out of the region

$$\Omega = [\max\{0, \delta_\ell - r_e\}, r_e + \delta_\ell). \tag{24}$$

Thus, we can explicitly state

$$g_n(\rho) = \begin{cases} 2\bar{\phi}_{\delta_\ell}(\rho)\mathrm{sinc}(n\bar{\phi}_{\delta_\ell}(\rho)), & \text{for } \rho \in \Omega \\ 0, & \text{otherwise} \end{cases}. \tag{25}$$

This form conveys the piecewise behavior of $g_n(\rho)$. Interestingly, $g_n(\rho)$ is also the Radon transform of the radial part of the Zernike polynomial $R^{n-1}_{n-1}(\rho)$, with integral transform representation as given by $\mathcal{R}\{R^{n-1}_{n-1}(\rho);\zeta_{\delta_\ell}(\rho)\} = (-1)^{\frac{n-1}{2}}\int_{-\infty}^{\infty}\frac{J_n(t)}{t}e^{i\zeta_{\delta_\ell}(\rho)t}\mathrm{d}t$ [29].

Finally, setting $\varphi(r,\theta) = \varphi_o(r,\theta) + \varphi_\ell$ and substituting Eq. (23) in Eq. (20), we have for arbitrary main lens transmission functions

$$U^s_\ell(r,\theta) = \sum_{p,q} i^{|q|}\beta^q_p e^{iq\varphi_\ell}\left(\sum_{s=-\infty}^{\infty} i^s e^{is\varphi(r,\theta)}\mathcal{H}_s\{u^q_{ps}(\rho);\gamma_o(r,\theta)\}\right). \tag{26}$$

A small number of terms over the series for p, q indices is generally enough for small aberrations and minimal main lens vignetting. It may be shown that considerable simplification can be made toward the ideal plenoptic 1.0 setup or an aberration-free imaging system. The latter case will hold for a high-quality main lens whose optical elements are well aligned from the manufacturing process. Somewhat more generally, under the circumstance that U solely depends on ρ, then $\beta^q_p = 0$, $\forall q \neq 0$. We can now half the number of terms in the series required to attain the same level of accuracy, by identifying the asymmetric relation between terms of opposite index entry. For $q = 0$, it is easy to show that, as $g_{-s}(\rho) = g_s(\rho)$,

$$u^0_{p(-s)}(\rho) = u^0_{ps}(\rho). \tag{27}$$

Therefore, exploiting the asymmetric property of Bessel functions $J_{-s}(x) = (-1)^s J_s(x)$, we may easily find

$$\mathcal{H}_{-s}\{u^0_{p(-s)}(\rho);\gamma_o(r,\theta)\} = (-1)^s\mathcal{H}_s\{u^0_{ps}(\rho);\gamma_o(r,\theta)\}. \tag{28}$$

Splitting the series expression of the LF-PSF, for negative indices in s, changing the index of summation $s \to -s$, we find

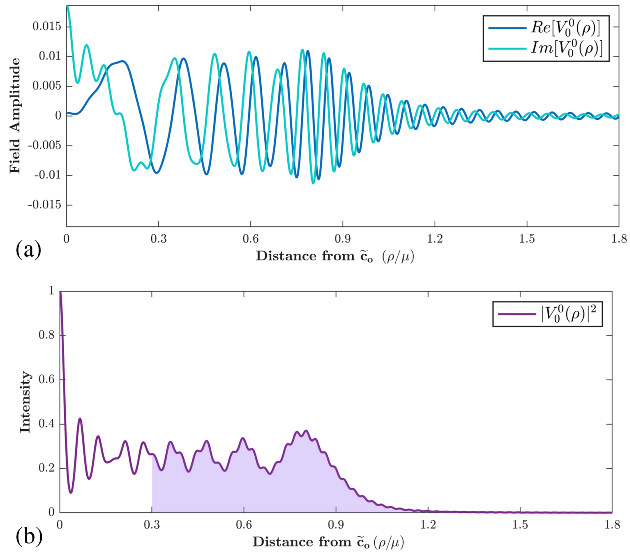

Fig. 4. (a) Exemplary real and imaginary parts of the incident amplitude distribution $V^0_0(\rho)$ for strong defocusing with respect to the MLA. (b) Corresponding intensity distribution $|V^0_0(\rho)|^2$. Radial coordinate ρ is normalized with respect to the geometric spot radius given by the formula $\mu = aR_e\left(\frac{1}{z_o}+\frac{1}{a}-\frac{1}{f_L}\right)$. Shading depicts the illuminated region of the microlens.

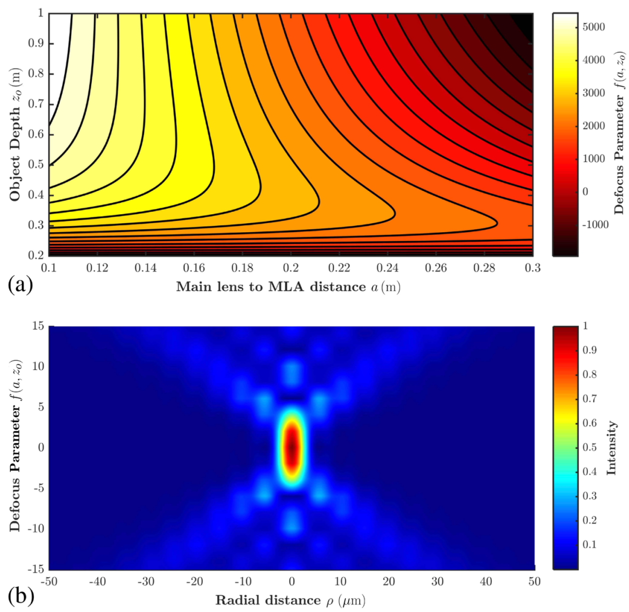

Fig. 5. (a) Contour plot of the defocus parameter $f(a, z_o)$ and (b) a focal stack of aberration-free intensity PSFs $|V^0_0(\rho)|^2$ for an example main lens.

$$\sum_{s=-\infty}^{-1} i^s e^{is\varphi(r,\theta)}\mathcal{H}_s\{u^0_{ps}(\rho);\gamma_o(r,\theta)\}$$

$$=\sum_{s=1}^{\infty}(-1)^s i^{-s} e^{-is\varphi(r,\theta)}\mathcal{H}_s\{u^0_{ps}(\rho);\gamma_o(r,\theta)\}. \quad \textbf{(29)}$$

So the intensity LF-PSF $I^s_\ell(r,\theta)=|U^s_\ell(r,\theta)|^2$, using Eq. (26) gives

$$I^s_\ell(r,\theta)\propto\left|\sum_p\sum_{s=0}^{\infty}\epsilon_s\beta^0_p i^s\cos(s\varphi(r,\theta))\mathcal{H}_s\left\{u^0_{ps}(\rho);\gamma_o(r,\theta)\right\}\right|^2, \quad \textbf{(30)}$$

with $\epsilon_s=2-\delta_{s0}$, δ_{nm} being the Kronecker delta tensor.

If we consider, for example, an aberration-free thin main lens with a clear circular pupil function and aperture stop at the lens, we have $\beta^0_p=0$, $\forall p\neq 0$. The ENZ theory then gives (see Figs. 4 and 5)

$$V^0_0(\rho')=e^{if/2}\sum_{\ell=0}^{\infty}(-i)^\ell(2\ell+1)j_\ell(f/2)\frac{J_{2\ell+1}(2\pi c_{z_o}\rho')}{2\pi c_{z_o}\rho'}, \quad \textbf{(31)}$$

Where, as formerly derived in [17] for small image side numerical aperture, $\mathrm{NA}'=R_e/z'_o$, while the transversal scaling factor c_{z_o} and defocus parameter that now reduces to $f=\pi(p'_o-a)\mathrm{NA}'^2/\lambda$, may both be expressed as

$$c_{z_o}=\frac{R_e}{\lambda}\left(\frac{1}{f_L}-\frac{1}{z_o}\right),$$

$$f=\frac{\pi a R_e^2}{\lambda}\left(\frac{1}{f_L}-\frac{1}{z_o}\right)\left(\frac{1}{a}-\frac{1}{f_L}+\frac{1}{z_o}\right), \quad \textbf{(32)}$$

respectively, and j_ℓ is the spherical Bessel functions of the first kind, R_e is the radius of the main lens, z_o is the distance of the object to the main lens, and f_L is the focal length of the main lens. Therefore, the aberration-free LF camera yields an intensity response

$$I^s_\ell(r,\theta)=\mathscr{C}_{\delta_\ell}\left|\sum_{s=0}^{\infty}\epsilon_s i^s\cos(s\varphi(r,\theta))\mathcal{H}_s\{u^0_{0s}(\rho);\gamma_o(r,\theta)\}\right|^2, \quad \textbf{(33)}$$

where $\mathscr{C}_{\delta_\ell}$ is a suitable power transmission coefficient derived in Appendix B. In general, $I^s_\ell(r,\theta)$ is asymmetric due to the nature of the amplitude distribution incident on the microlenses, as shown in Figs. 6 and 7. A spatially variant asymmetric PSF consequence of this would explain at least in part the distortions that give rise to the curvilinear epipolar lines on the local scale of the microimages. It is also essential to emphasize that the solutions, as provided by Eqs. (26), (30), and (33), are not restricted to an APSF incident on the MLA to be of the form given by the ENZ theory. Indeed, any expansion of the form of U above renders the equations valid. Furthermore, the expressions above for the LF-PSF can be further simplified under field approximations corresponding to the small and large defocus limits at the MLA.

For $\delta_\ell\gg r_e$, the rate of convergence of the series as given by Eqs. (26), (30), and (33) deteriorates significantly. In cases where the redundancy is high and in which many microlenses

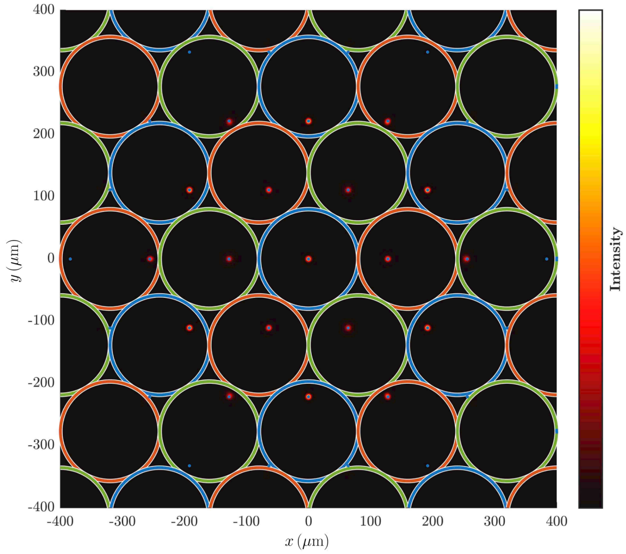

Fig. 6. LF-PSFs for an in-focus point source with a single microlens type MLA. The blue dots are the ideal image points $\boldsymbol{x}^{\mathrm{ideal}}_\ell$.

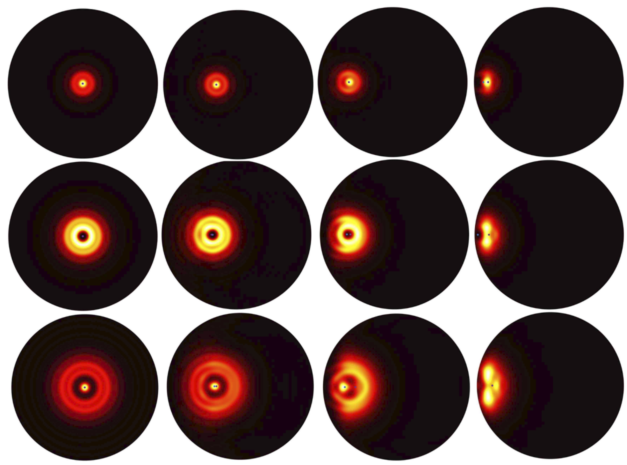

Fig. 7. Columns (left to right) show the set of LF-PSFs for values of $\delta_\ell=0,\ldots\mu+r_e$ at uniform intervals for an aberration-free, circular clear pupil for the main lens, demonstrating increasing asymmetry and distortion in the LF-PSF. The point source is displaced along the positive x direction. The blue dots represent the ideal image points $\boldsymbol{x}^{\mathrm{ideal}}_\ell$ and the purple dots represent the LF-PSF centroids, which are the real image points. As shown in each microimage, showing increasing divergence as the defocusing and vignetting is enhanced. For realistic comparison, the plots are normalized relative to the total energy transmitted through the lens, as given by the power transmission coefficient $\mathscr{C}_{\delta_\ell}$.

observe the scene point, an alternative expression as derived in Appendix C describes a method for a good approximation of the irradiance distribution observed at the sensor.

3. SYMMETRY PROPERTIES OF THE LF-PSF

By re-expressing the intensity LF-PSF in an alternative shifted coordinate frame, we are able to enhance computational efficiency by reducing the necessary computations of the Hankel transforms in Eq. (33). In the unique alternate coordinate frame

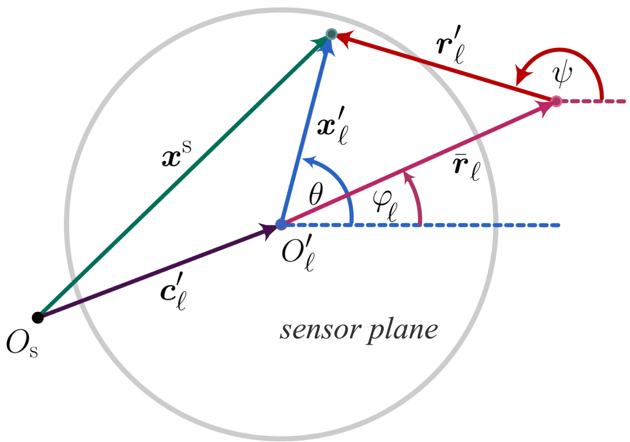

Fig. 8. Geometry illustrating the relations of the observation vector for evaluation of the LF-PSF $\boldsymbol{x}'_\ell$ measured relative to O'_ℓ, the position vector of the main lens chief ray intersection with the sensor $\bar{\boldsymbol{r}}_\ell$ and the new observation vector $\boldsymbol{r}'_\ell$ in the shifted coordinate frame, defined by the linear transform $\boldsymbol{r}'_\ell = \boldsymbol{x}'_\ell - \bar{\boldsymbol{r}}_\ell$.

$\boldsymbol{r}'_\ell = \boldsymbol{x}'_\ell - \bar{\boldsymbol{r}}_\ell$, as shown in Fig. 8, in which we define polar coordinates (ε, ψ), where $\varepsilon = |\boldsymbol{r}'_\ell|$ and $\psi = \arg\{\boldsymbol{r}'_\ell\}$, we are able to express the LF-PSF as an infinite series of separable functions of radial and angular dependency. Specifically, the Hankel transforms become solely of radial dependency, which means that these integral transforms do not need to be iteratively computed for all points in the sensor that are bounded by the microimage because circles centered on $\boldsymbol{x}^s_o = \boldsymbol{c}'_\ell + \bar{\boldsymbol{r}}_\ell$ define contours of the Hankel tranforms.

In this shifted coordinate frame (ε, ψ), the simplified expression for the LF-PSF immediately reveals the inherent mirror symmetry property of the irradiance distribution about the axis of polar angle φ_ℓ through the origin of the (ε, ψ) frame.

The functions φ and γ_o now transform to $\varphi(\psi) = \varphi_\ell - \psi - \pi$ and $\gamma_o(\varepsilon) = \frac{k}{b}\varepsilon$. Thus Eq. (33) can now be expressed as

$$I^s_\ell(\varepsilon, \psi) = \mathscr{C}_{\delta_\ell} \left| \sum_{s=0}^{\infty} \epsilon_s (-i)^s \cos(s(\psi - \varphi_\ell)) \mathcal{H}_s\{u^0_{0s}(\rho); \gamma_o(\varepsilon)\} \right|^2, \tag{34}$$

where $\mathcal{H}_s\{u^0_{0s}(\rho); \gamma_o(\varepsilon)\} = \int_0^\infty u^0_{0s}(\rho) J_s\left(\frac{k\varepsilon\rho}{b}\right)\rho \mathrm{d}\rho$. It therefore is immediately clear that the irradiance obeys the mirror symmetry property $I^s_\ell(\varepsilon, \varphi_\ell + \psi) = I^s_\ell(\varepsilon, \varphi_\ell - \psi)$ for $\psi \in [0, 2\pi)$. More crucially, however, the origin of the (ε, ψ) frame is situated on the axis of polar angle φ_ℓ through the microimage center O'_ℓ. This is because the origin of (ε, ψ) has a position vector with respect to O'_ℓ of $\bar{\boldsymbol{r}}_\ell$ that is collinear to $\boldsymbol{\delta}_\ell$ where $\varphi_\ell = -\arg\{\boldsymbol{\delta}_\ell\}$. Therefore, it follows that the irradiance is also mirror symmetric in the fixed coordinate frame (r, θ) independent of $\boldsymbol{\delta}_\ell$, with

$$I^s_\ell(r, \varphi_\ell + \theta) = I^s_\ell(r, \varphi_\ell - \theta). \tag{35}$$

The same simplification through the use of the coordinate transform above applies to Eq. (26). However, in this new coordinate frame, the general variation of the vector $\boldsymbol{\delta}_\ell$ will typically lead to an inhomogeneous sampling for evaluation of the irradiance within the microimage; thus, one should take caution in simulating the LF-PSFs to avoid artifacts in the rendered images.

Using these properties of symmetry, we can conclude that given an LF camera with an optical setup strictly confined to paraxial imaging, which may include a LF microscope with a telecentric objective-tube lens setup acting as the main lens, if the position of the object point is such that $\boldsymbol{\delta}_\ell$ takes the same magnitude and angle, independent of indices ℓ, then the relative intensity distribution $I^s_\ell(r, \theta)$ remains invariant. This defines the diffractive periodicity between microimages and implies that it is sufficient to consider all responses under any one given microlens because its collective set of responses is invariant from microimage to microimage. By itself, this property may be exploited to increase the computational efficiency by the factor of the ratio of the total number of microlenses to the number of microlens types.

Furthermore, the diffractive mirror symmetry property that was shown to hold true above from analysis is not only in congruence with the light field centroid (LFC) theorem in [15], but it has the more profound implication in that the centroids of the PSF can only be radially displaced with respect to the microimage center.

Moreover, there exists a rotational property of the response in the plenoptic camera. In mathematical terms,

$$I^s_\ell(r, \theta + \Delta\varphi_\ell)\big|_{\boldsymbol{R}(\Delta\varphi_\ell)\boldsymbol{\delta}_\ell} = I^s_\ell(r, \theta)\big|_{\boldsymbol{\delta}_\ell}, \tag{36}$$

where $\boldsymbol{R}(\Delta\varphi_\ell)$ is the rotation matrix that, upon operation, rotates the vectors counterclockwise by the angle $\Delta\varphi_\ell$. If both Eqs. (35) and (36) hold true, then the microimage radial distortions are isotropic.

It has been further proven in [15] that the same properties stated above hold true for any radially symmetric deformation of the main lens caustic that remains transversally shift invariant. So, given these results, for any LF camera configured under the same conditions, all possible cases may be comprehended for the LF-PSF for a fixed depth plane by considering points along a single radial path within a single microlens's field of view to its edge; i.e., consider simulations of the LF-PSF for $\delta_\ell \in [0, \mu + r_e)$ where μ is the geometrical spot radius in the plane of the MLA. Considering $\delta_\ell \geq \mu + r_e$ from the perspective of geometrical optics, no rays intersect the microlens aperture and the light is completely vignetted by the main lens.

It is important to emphasize that the conclusions reached regarding the periodicity of microimages, rotational property, and mirror symmetry of the LF-PSF are exact results assuming the conditions of a telecentric main lens or assuming a main lens satisfying paraxial imaging with the microlenses satisfying the Fresnel approximation. However, one more statement may be made in the more general case of a circularly symmetric main lens with a severely decentered microlens that departs from the paraxial regime, giving rise to off-axis aberrations. When we define $\vartheta_\ell = \arg\{\boldsymbol{c}'_\ell\}$, then we claim

$$I^s_\ell(r, \vartheta_\ell - \theta)\big|_{\boldsymbol{R}(2(\vartheta_\ell - \varphi_\ell))\boldsymbol{\delta}_\ell} = I^s_\ell(r, \vartheta_\ell + \theta)\big|_{\boldsymbol{\delta}_\ell}. \tag{37}$$

This equivalently says that if $\boldsymbol{\delta}_\ell$ is transformed only by a counterclockwise rotation of $2(\vartheta_\ell - \varphi_\ell)$, then the LF-PSF is reflected about the line of polar angle ϑ_ℓ through O_ℓ. More generally, this means that the set of all LF-PSFs under a given

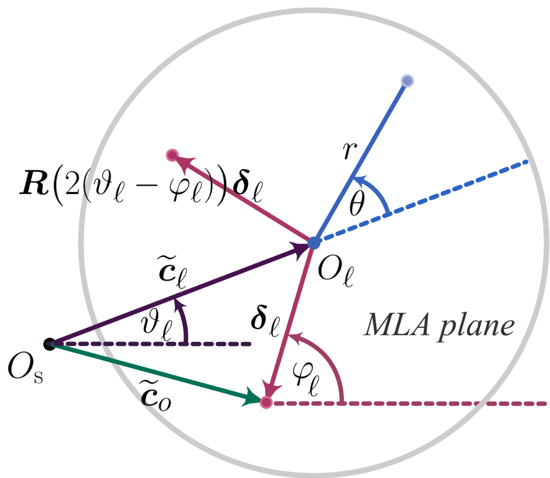

Fig. 9. Vectorial representation of rotation of $\boldsymbol{\delta}_\ell$ anti-clockwise by $2(\vartheta_\ell - \varphi_\ell)$ in the image formation reflects the LF-PSF about the axis of polar angle ϑ_ℓ for a decentered microlens. In both diagrams, O_s is where the main lens optical axis intersects the sensor plane, O'_ℓ is the lateral coordinates of the corresponding microimage center.

microimage are mirror symmetric about the axis through O_ℓ inclined at polar angle ϑ_ℓ. This result should remain valid, assuming that the refractive elements and aperture stop constituting the main lens and microlenses, are individually, as subsystems, well-aligned and comprise rotational symmetry, as shown in Fig. 9.

4. COMPARISON TO RAYLEIGH–SOMMERFELD MODEL

To truly test the validity of the semi-analytical solution to the LF-PSF, comparison may be made with either experimental data, or with the gold standard theory of diffraction optics: the solution as given by the Rayleigh–Sommerfeld (RS) diffraction integral. For this model, the amplitude light distribution onto the sensor plane after a microlens, neglecting scalar pre-factors, takes

$$U^s_\ell(\boldsymbol{x}_\ell) = \iint_{\mathbb{R}^2} U^+_\ell(\boldsymbol{x}) \left(\frac{1}{R(\boldsymbol{x};\, \boldsymbol{x}_\ell)} - ik \right) \frac{e^{ikR(\boldsymbol{x};\boldsymbol{x}_\ell)}}{(R(\boldsymbol{x};\, \boldsymbol{x}_\ell))^2} \mathrm{d}^2\boldsymbol{x}, \tag{38}$$

with $U^+_\ell(\boldsymbol{x})$ given by Eq. (4), and where $R(\boldsymbol{x};\, \boldsymbol{x}_\ell) = \sqrt{|\boldsymbol{x} - \boldsymbol{x}_\ell|^2 + b^2}$. Introducing again the polar coordinates in the microlens exit pupil and sensor plane (υ, ω) and (r, θ), respectively, where $\upsilon = |\boldsymbol{x}|$ and $\omega = \arg\{\boldsymbol{x}\}$, $r = |\boldsymbol{x}_\ell|$ and $\theta = \arg\{\boldsymbol{x}_\ell\}$, we obtain

$$U^s_\ell(r, \theta) = \int_0^{2\pi} \int_0^{\infty} U\left(\frac{\upsilon}{M_p}, \omega, a;\, p_o\right) P_{n_\ell}(\upsilon, \omega)$$
$$e^{-i\frac{k}{2f_{n_\ell}}\upsilon^2} e^{i\frac{k}{M_p a}\left|\frac{\boldsymbol{\delta}_\ell}{M_p} + \widetilde{\boldsymbol{c}}_\ell - \boldsymbol{c}_e\right|\upsilon\cos(\omega - \omega_\ell)}$$
$$\left(\frac{1}{R(\upsilon, \omega;\, r, \theta)} - ik\right) \frac{e^{ikR(\upsilon,\omega;r,\theta)}}{(R(\upsilon, \omega;\, r, \theta))^2} \upsilon \mathrm{d}\upsilon \mathrm{d}\omega, \tag{39}$$

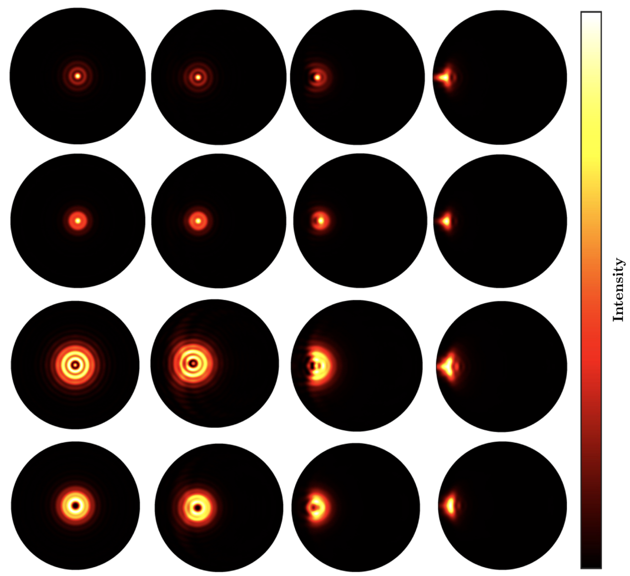

Fig. 10. Comparison of the Fresnel approximation and the exact R-S integrals in diffraction consideration from the microlens for two distinct defocus values, with geometric defocus at the sensor of $\mu^s_{\mathrm{geo}} = 10$ µm and $\mu^s_{\mathrm{geo}} = 15$ µm, respectively, and a main lens defocus at the MLA of $\mu = 1.65 r_e$ and $\mu = 1.35 r_e$. Simulations are rendered for a system with physical parameter values of $R_e = 1$ cm, $r_e = 75$ µm, $f_L = 10$ cm, $f_{n_\ell} = 3$ mm, $a = 26.9$ cm, and $b = 2$ mm. The microlens has a small Fresnel number of $N_F \approx 5$. Odd rows are simulated using Eq. (40) with the exact R-S integral, while even rows are simulated using Eq. (33) with the Fresnel approximation. Evidently the fringes are somewhat more pronounced in the simulation using the exact R-S integral solution to the LF-PSF, with marginal focal shift effect due to the small Fresnel number of the microlens. Aside from this, the Fresnel approximation clearly serves as a good approximation to the R-S diffraction integral.

where $R(\upsilon, \omega;\, r, \theta) = \sqrt{r^2 + \upsilon^2 - 2r\upsilon\cos(\omega - \theta) + b^2}$ and $\omega_\ell = \arg\{\frac{\boldsymbol{\delta}_\ell}{M_p} + \widetilde{\boldsymbol{c}}_\ell - \boldsymbol{c}_e\}$. Let us suppose once again that the main lens APSF incident on the MLA is aberration-free as given by the $V^0_0(\rho')$ function from the ENZ theory. Then we have

$$U^s_\ell(r, \theta) = \int_0^{2\pi} \int_0^{\infty} V^0_0\left(\frac{\mathrm{NA}'}{\lambda M_p}\sqrt{\upsilon^2 + \delta^2_\ell + 2\delta_\ell\upsilon\cos(\omega - \varphi_\ell)}\right)$$
$$P_{n_\ell}(\upsilon, 0) e^{-i\frac{k}{2f_{n_\ell}}\upsilon^2} e^{i\frac{k}{M_p a}\left|\frac{\boldsymbol{\delta}_\ell}{M_p} + \widetilde{\boldsymbol{c}}_\ell - \boldsymbol{c}_e\right|\upsilon\cos(\omega - \omega_\ell)}$$
$$\left(\frac{1}{R(\upsilon, \omega;\, r, \theta)} - ik\right) \frac{e^{ikR(\upsilon,\omega;r,\theta)}}{(R(\upsilon, \omega;\, r, \theta))^2} \upsilon \mathrm{d}\upsilon \mathrm{d}\omega. \tag{40}$$

This is the final expression of the irradiance distribution in the sensor plane for an aberration-free system for a main lens under the Debye approximation and for a microlens under the Rayleigh–Sommerfeld integral. Figure 10 shows a comparison of the simulation results from Eq. (33) and (40), which clearly confirms the high accuracy of the model. The similarity in the fringe patterns and the defocus demonstrates this fact. The slightly stronger defocus predicted by the RS integral can be explained by the focal shift effect.

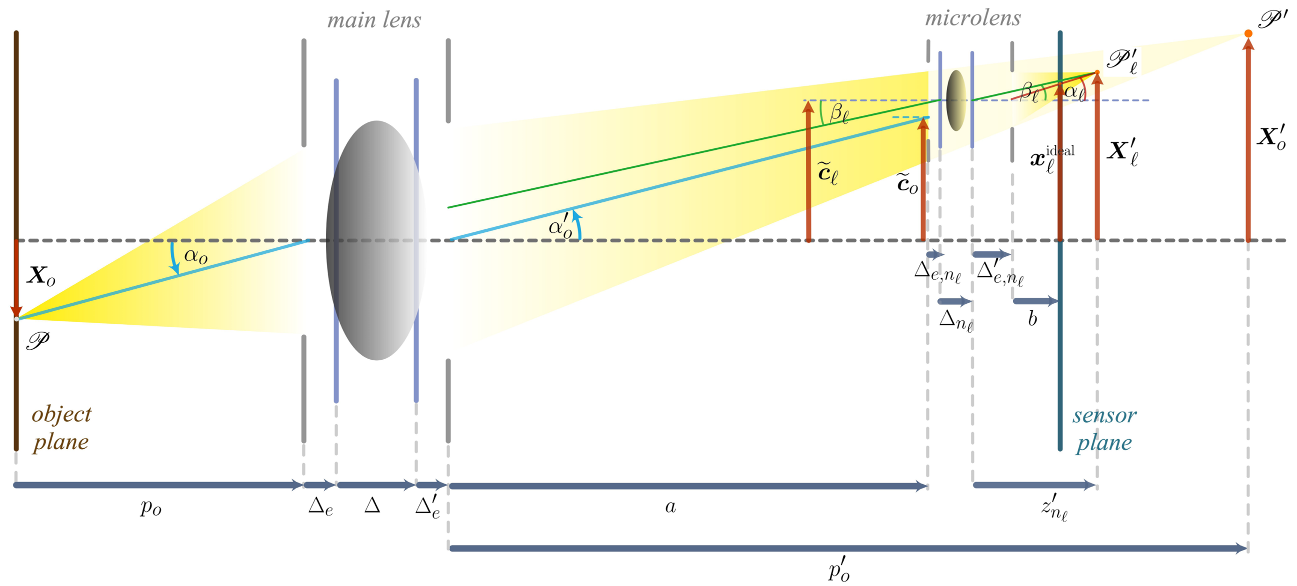

Fig. 11. Schematic of ray geometry of the image formation in a plenoptic camera. An object point $\mathscr{P}$ is imaged from Π_o by the main lens forming the intermediate (virtual) image at $\mathscr{P}'$, which is then imaged by the microlens to produce the focused image at $\mathscr{P}'_\ell$. The pupil planes of the main lens and microlens are shaded in gray, while principal planes are shaded in blue. The main lens chief ray intersects the center of the main lens pupils and spans an angle of α_o and α'_o in object and image space, respectively, in reference to the optical axis. The image observed at the sensor Π_s has position vector $\boldsymbol{x}_\ell^{\text{ideal}}$ and is defined by the microlens chief ray which intersects both the microlens exit pupil and $\mathscr{P}'_\ell$.

5. DIFFRACTIVE DISTORTION CONSEQUENT OF VIGNETTING

What makes the vignetting problem particularly interesting in the LF camera is that, contrary to aberrations, vignetting is not rectifiable but is rather an inherent property of the system. One practical application of a diffraction model is to assess the nature of distortion due to vignetting. For us to isolate and determine the significance of vignetting on distortion, the analysis shall be restricted to the aberration-free system. This is useful because it allows us to comprehend and approximate the general dependencies of this form of distortion on systematic parameters. To determine and assess the presence of distortion, it is necessary to consider the first-order moment or center of mass of the intensity PSF, measured relative to the ideal image point. Figure 11 shows an illustration of the image formation in the case of a system composed solely of a thin lenses. For a general thick lens microlens, the vector coordinates for the ideal image points $\boldsymbol{x}_\ell^{\text{ideal}}$ are obtained by tracing the chief ray through the center of the microlens's exit pupil to the sensor. Therefore, given the microlens image point $\boldsymbol{X}'_\ell$ it must generally follow from the geometry that

$$\boldsymbol{x}_\ell^{\text{ideal}} = \tilde{\boldsymbol{c}}_\ell + \frac{b\left(\boldsymbol{X}'_\ell - \tilde{\boldsymbol{c}}_\ell\right)}{z'_{n_\ell} - \Delta'_{e,n_\ell}}, \tag{41}$$

where z'_{n_ℓ} is the distance of the microlens' image distance from its second principal plane, and Δ'_{e,n_ℓ} is the microlens' second principal plane to the exit pupil distance. The microlens image point forms along the emergent ray through the second principle point. This ray is also parallel to the ray through the microlens' first principal point, giving

$$\boldsymbol{X}'_\ell = \tilde{\boldsymbol{c}}_\ell + \frac{z'_{n_\ell}\left(\boldsymbol{X}'_o - \tilde{\boldsymbol{c}}_\ell\right)}{p'_o - a - \Delta_{e,n_\ell}}, \tag{42}$$

where p'_o is the image distance of the main lens from its exit pupil and Δ_{e,n_ℓ} is the microlens' entrance pupil to the first principal plane distance. The main lens' intermediate image point may also be expressed by the linear projection $\boldsymbol{X}'_o = p'_o(\tilde{\boldsymbol{c}}_o - \boldsymbol{c}_e)/a + \boldsymbol{c}_e$ where $\boldsymbol{c}_e$ is the center of the effective exit pupil of the main lens and in general may depend on the object point coordinates. By eliminating $\boldsymbol{X}'_\ell$ in Eq. (41) and $\boldsymbol{X}'_o$ in Eq. (42) with the formulas above, we may write $\boldsymbol{x}_\ell^{\text{ideal}}$ solely in terms of the vectors $\tilde{\boldsymbol{c}}_o$, $\tilde{\boldsymbol{c}}_\ell$, and $\boldsymbol{c}_e$ as

$$\boldsymbol{x}_\ell^{\text{ideal}} = \tilde{\boldsymbol{c}}_\ell + \kappa\left[p'_o(\tilde{\boldsymbol{c}}_o - \boldsymbol{c}_e) - a(\tilde{\boldsymbol{c}}_\ell - \boldsymbol{c}_e)\right], \tag{43}$$

where $\kappa = b/[a(1 - \Delta'_{e,n_\ell}/z'_{n_\ell})(p'_o - a - \Delta_{e,n_\ell})]$. By the conjugate equation, $1/f_{n_\ell} = 1/z'_{n_\ell} - 1/(p'_o - a - \Delta_{e,n_\ell})$, allowing us to eliminate z'_{n_ℓ} in κ, yields

$$\kappa = \frac{b}{a\left[\left(1 - \Delta'_{e,n_\ell}/f_{n_\ell}\right)\left(p'_o - a - \Delta_{e,n_\ell}\right) - \Delta'_{e,n_\ell}\right]}. \tag{44}$$

By now defining the center of the microimage $\boldsymbol{c}'_\ell$ as the image point formed when the main lens and microlens chief ray are equivalent (i.e., $\boldsymbol{c}'_\ell = \boldsymbol{x}_\ell^{\text{ideal}}|_{\delta_\ell=0}$), then

$$\boldsymbol{c}'_\ell = \tilde{\boldsymbol{c}}_\ell + \kappa\,(p'_o - a)\,(\tilde{\boldsymbol{c}}_\ell - \bar{\boldsymbol{c}}_e)\,. \tag{45}$$

Above, $\bar{\boldsymbol{c}}_e$ is the center of the effective exit pupil of the main lens for this special case. Note that in [17], this was derived for a thin microlens with the stop at the lens; i.e., where $\Delta_{e,n_\ell} = \Delta'_{e,n_\ell} = 0$. These approximations simplify Eq. (45) to $\boldsymbol{c}'_\ell = \left(1 + \frac{b}{a}\right)\boldsymbol{c}_\ell - \frac{b}{a}\bar{\boldsymbol{c}}_e$. By expressing the ideal image coordinates in terms of the microimage center as given by Eq. (45),

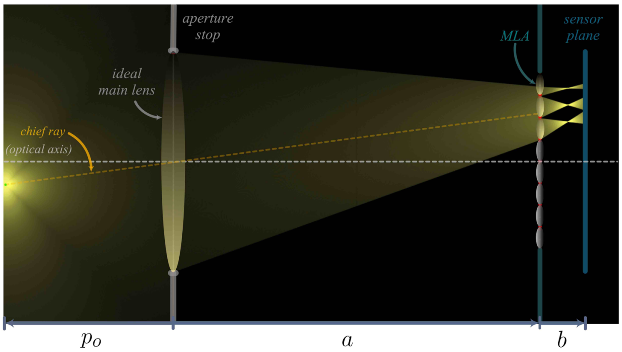

Fig. 12. Schematic of the imaging of an aberration-free plenoptic camera composed of an ideal (thin) main lens and thin microlenses with stops at the lenses. The diagram illustrates how the ray geometry of Fig. 11 is reduced when the distances $\Delta = \Delta_e = \Delta'_e = 0$ and $\Delta_{n_\ell} = \Delta_{e,n_\ell} = \Delta'_{e,n_\ell} = 0$ with $M_p = 1$.

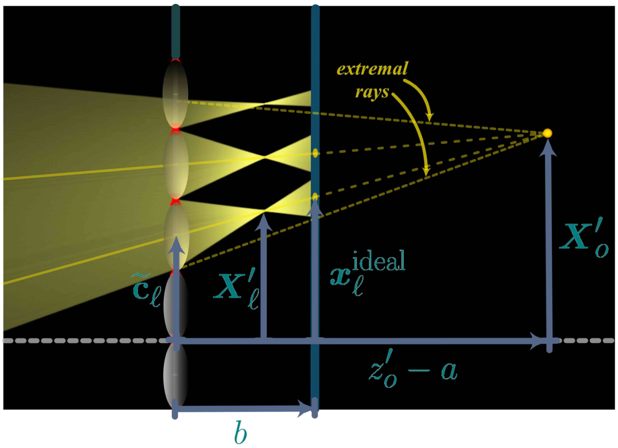

Fig. 13. Figure depicting a corresponding zoom upon the illuminated region of the MLA, with the top most microlens subject to main lens vignetting.

Eq. (43) may be rewritten as

$$\boldsymbol{x}^{\text{ideal}}_\ell = \boldsymbol{c}'_\ell - \kappa\left[(p'_o - a)(\boldsymbol{c}_e - \bar{\boldsymbol{c}}_e) - p'_o \boldsymbol{\delta}^-_\ell\right], \tag{46}$$

with $\boldsymbol{c}'_\ell$ as given by Eq. (45) in the general case.

Once again, when the parameters $\Delta_{e,n_\ell} = \Delta'_{e,n_\ell} = 0$, we obtain $\kappa = b/[a(p'_o - a)]$, which simplifies Eq. (46) to

$$\boldsymbol{x}^{\text{ideal}}_\ell = \boldsymbol{c}'_\ell + \frac{b}{a}(\bar{\boldsymbol{c}}_e - \boldsymbol{c}_e) + \frac{b p'_o}{a(p'_o - a)}\boldsymbol{\delta}^-_\ell . \tag{47}$$

There are two important types of optical systems to be considered that are of frequent interest in light field photography.

Case I: In the presence of a thin main lens with the stop at the lens, $\boldsymbol{c}_e \equiv \bar{\boldsymbol{c}}_e = 0$, yielding $\boldsymbol{x}^{\text{ideal}}_\ell = \left(1 + \frac{b}{a}\right)\widetilde{\boldsymbol{c}}_\ell + \kappa\, p'_o \boldsymbol{\delta}^-_\ell$.

Setting $\Delta_{e,n_\ell} = \Delta'_{e,n_\ell} = 0$, the image point reduces further to

$$\boldsymbol{x}^{\text{ideal}}_\ell = \left(1 + \frac{b}{a}\right)\widetilde{\boldsymbol{c}}_\ell + \frac{b z'_o}{a(z'_o - a)}\boldsymbol{\delta}^-_\ell , \tag{48}$$

where z'_o is the image distance of the main lens from the plane of the lensas shown in Figures 12 and 13.

Case II: Alternatively, for a telecentric main lens, $\boldsymbol{c}_e = \widetilde{\boldsymbol{c}}_o$ and $\bar{\boldsymbol{c}}_e = \widetilde{\boldsymbol{c}}_\ell$, for which Eq. (46) gives $\boldsymbol{x}^{\text{ideal}}_\ell = \widetilde{\boldsymbol{c}}_\ell + \kappa a \boldsymbol{\delta}^-_\ell$ as $\boldsymbol{c}'_\ell = \widetilde{\boldsymbol{c}}_\ell$.

Again, if $\Delta_{e,n_\ell} = \Delta'_{e,n_\ell} = 0$, then

$$\boldsymbol{x}^{\text{ideal}}_\ell = \widetilde{\boldsymbol{c}}_\ell + \frac{b}{p'_o - a}\boldsymbol{\delta}^-_\ell . \tag{49}$$

In general, for notational convenience and clarity, all unit vectors from now on shall be ascribed with a hat symbol.

Now, define $\boldsymbol{r}_\ell = \boldsymbol{x}^{\text{ideal}}_\ell - \boldsymbol{c}'_\ell$ and $\hat{\boldsymbol{r}}_\ell = \boldsymbol{r}_\ell / |\boldsymbol{r}_\ell|$ as its unit vector. Then observe that $\hat{\boldsymbol{\delta}}_\ell = \epsilon \hat{\boldsymbol{r}}_\ell$, $\hat{\boldsymbol{\delta}}_\ell \cdot \hat{\boldsymbol{r}}_\ell = \epsilon$, where $\epsilon = \operatorname{sign}(\kappa)$ when the general equations for the image point hold in case I and case II above. If $\boldsymbol{x}^{\text{ideal}}_\ell$ may be further simplified to either Eq. (48) or Eq. (49), then $\epsilon = \operatorname{sign}(p'_o - a)$.

By definition, the distortion vector is the displacement from the ideal image point to the true image point; i.e., $\boldsymbol{v}_\ell = \boldsymbol{x}^{\text{obs}}_\ell - \boldsymbol{x}^{\text{ideal}}_\ell$. From the LFC theorem, since the diffraction pattern has a mirror symmetry along the line of polar angle φ_ℓ through the microimage center O'_ℓ with vector coordinates $\boldsymbol{c}'_\ell$, then the center of mass of irradiance has a position vector of the form $\boldsymbol{e}^s_\ell = e^s_\ell \hat{\boldsymbol{r}}_\ell$, where $\boldsymbol{x}^{\text{obs}}_\ell = \boldsymbol{c}'_\ell + \boldsymbol{e}^s_\ell$. Using these formulas and, by definition of $\boldsymbol{v}_\ell$, we finally obtain

$$\boldsymbol{v}_\ell = (e^s_\ell - \kappa\, p'_o)\hat{\boldsymbol{r}}_\ell, \quad \boldsymbol{v}_\ell = (e^s_\ell - \kappa a)\hat{\boldsymbol{r}}_\ell,$$

$$e^s_\ell = \frac{\int_0^{2\pi}\int_0^\infty r^2 \cos(\theta - \psi) I^s_\ell(r, \theta) \mathrm{d}r \mathrm{d}\theta}{\int_0^{2\pi}\int_0^\infty I^s_\ell(r, \theta) r \mathrm{d}r \mathrm{d}\theta}, \tag{50}$$

which are the two corresponding distortion equations, respectively, for $\boldsymbol{v}_\ell$ when the image point is described by the general equations of case I and case II.

Above, we define $\psi = \varphi_\ell - \pi\, \chi_{[a,\infty)}(p'_o)$. Having expressed the distortion vector $\boldsymbol{v}_\ell$ in terms of the radial unit vector $\hat{\boldsymbol{r}}_\ell$, the sign of $\boldsymbol{v}_\ell$ is indicative of the type of distortion characteristic in the microimage. According to geometric optics, the sign reverses according to the sign of defocus at the sensor plane in regions where the vignetting is significant. More specifically, a positive sign of distortion corresponds to a radially outward pincushion distortion, which is expected to occur when the final image of the microlens is real. On the other hand, a negative sign of distortion corresponds to a radially inward barrel distortion, in the case in which the final image of the microlens is virtual. The center of the microimage O'_ℓ, is the center of all such radial distortions from vignetting. Image points closest to O'_ℓ are least distorted due to minimal vignetting, while image points closer to the edge of the microimage, form with reduced illuminance and a stronger radial distortion with respect to O'_ℓ.

In Fig. 6, simulations elicit the potential formation of asymmetry in the LF-PSF, which becomes increasingly pronounced for a stronger defocus in the presence of vignetting, and gives a reason to suspect distortion from vignetting. In Fig. 14, the solid orange line curve representing the flux of irradiance transmitted through the microlens can be seen as a measure of this vignetting, which consequently leads to an increasing magnitude of distortion. This is calculated using Eq. (B2) from Appendix B. The dotted orange line curve corresponds to the encircled energy about the position vector $\boldsymbol{x}^{\text{ideal}}_\ell$ relative to O'_ℓ.

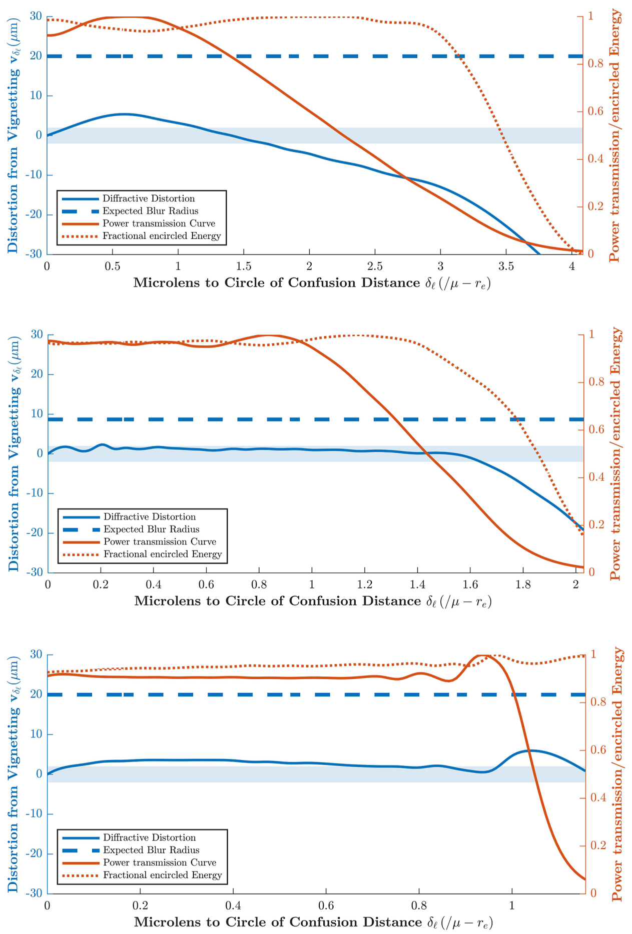

Fig. 14. Line curves depicting the dissipation of the transmitted radiant flux through the microlens aperture due to vignetting, the consequent encircled energy of the intensity PSF within the expected blur radius in the sensor plane and the corresponding diffractive distortion. The physical parameters of the considered system take the values $R_e = 1$ cm, $r_e = 75$ μm, $f_L = 10$ cm, $f_{n_\ell} = 3$ mm, $a = 26.9$ cm, and $b = 2$ mm. Three distinct defocus setting are considered: The top and bottom rows correspond to opposite signs of defocus that give an equal geometrical defocus in the sensor, while the middle row corresponds to the in-focus plane. The point source is then moved radially from the center of the microlens's field of view. The narrow blue banded region represents the region in which quantization may potentially dominate the effects of optical distortion.

Corresponding to the graphs of Fig. 14, the image of a rectilinear object under a microlens for these three defocus cases is illustrated in Fig. 15.

If μ^s_{geo} is the radius of the geometric blur in the sensor plane, then $\mu^s_{\text{geo}} = r_e|1 - b/(z'_{n_\ell} - \Delta'_{e,n_\ell})|$ by similar triangle geometry. For simplicity, we shall proceed with the analysis by assuming a thin microlens with the stop at the lens, so that $M_p = 1$ and $\Delta_{e,n_\ell} = \Delta'_{e,n_\ell} = 0$. Thus, we easily obtain $\mu^s_{\text{geo}} = r_e b|1/b + 1/(a - z'_o) - 1/f_{n_\ell}|$, having used the conjugate equation to eliminate z'_{n_ℓ}. Furthermore, since the radius of the Airy disk is given by $\mu^s_{\text{Airy}} = 0.61 b\lambda/r_e$, the encircled energy E^s of interest is the ratio of encircled energy within the expected blur radius $\mu^s = \max\{\mu^s_{\text{geo}}, \mu^s_{\text{Airy}}\}$, to the total energy of the LF-PSF within the sensor plane, as given by

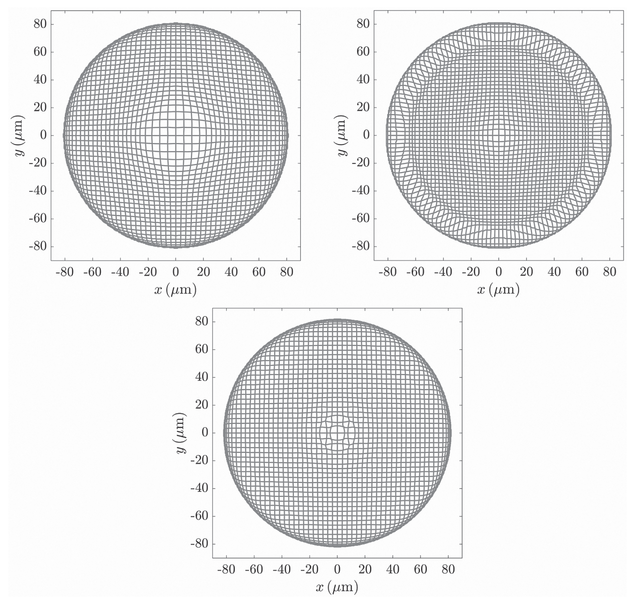

Fig. 15. Diffractive radial distortion corresponding to Fig. 14 in the order from top left to bottom, simulated for a single microimage when imaging a rectilinear object within the field of view of the microlens.

$$E^s(\varepsilon) = \frac{\int_0^{2\pi}\int_0^{\mu^s} I^s_\ell(\varrho, \vartheta; \varepsilon)\varrho \mathrm{d}\varrho \mathrm{d}\vartheta}{\int_0^{2\pi}\int_0^{\infty} I^s_\ell(\varrho, \vartheta; \varepsilon)\varrho \mathrm{d}\varrho \mathrm{d}\vartheta}, \tag{51}$$

where $I^s_\ell(\varrho, \vartheta; \varepsilon)$ represents the intensity response when the ideal image coordinates satisfy $\varepsilon = |\boldsymbol{x}^{\text{ideal}}_\ell - \boldsymbol{c}'_\ell|$, and (ϱ, ϑ) are polar coordinates centered on $\boldsymbol{c}'_\ell + \boldsymbol{x}^{\text{ideal}}_\ell$. The geometric defocus of the main lens μ is given by the projection of the main lens exit pupil to the MLA plane. Therefore, if the radius of the main lens exit pupil is R_e, we find from similar triangles that $\mu = R_e|1 - a/p'_o|$. When this defocus satisfies $\mu > r_e$, the microlenses always cause vignetting, while image points sufficiently near the border of the microimage also suffer from main lens vignetting. We may then define the region of vignetting of interest as corresponding to $\delta_\ell > \mu - r_e$ where $\delta_\ell = |\boldsymbol{\delta}_\ell|$. This corresponds to instances for which there is an asymmetric illumination of the microlens exit pupil due to only a partial overlap between the microlens and the illuminated region of the MLA. In the remaining region of $\delta_\ell \leq \mu - r_e$, the distortions are generally expected to be minimal due to a more homogenous illumination of the microlens entrance pupil. As it will be seen, the results confirm this for the setup considered.

As Fig. 14 shows, it generally holds true that $\boldsymbol{v}_\ell|_{\delta_\ell=0} = 0$, because the intensity LF-PSF is a radially symmetric distribution centered on the ideal image point. The severity of distortion becomes increasingly prominent and diverges in the negative direction from where the encircled energy $E^s(\varepsilon)$ deteriorates, until the system's response is no longer measurable. However, the δ_ℓ value for which the flux of irradiance transmitted through the microlens aperture deteriorates, does not necessarily serve as an accurate estimate of the point from which the distortion diverges. The same is true at the boundary $\delta_\ell = \mu - r_e$.

For the setup considered, when imaging the focus reference plane for which the geometric defocus $\mu^s_{\text{geo}} = 0$, we find that on the interval $\delta_\ell \leq \mu - r_e$, the distortion magnitude satisfies $v_\ell < 2.4 \ll 8$ μm $= \mu^s$. Therefore, relative to the microimage center with origin O'_ℓ, the centroid of irradiance has position coordinates $\boldsymbol{x}_\ell^{\text{obs}} \approx \boldsymbol{x}_\ell^{\text{ideal}}$. However, the mean and standard deviation of distortion magnitude on this interval are $\bar{v}_\ell = 1.5$ μm and $\sigma_{v_\ell} = 0.3$ μm, respectively. Both of these statistical quantities are on a subpixel scale in the absence of main lens vignetting.

So, if the point source lies in the focus reference plane, the model shows that, as expected, the diffraction spot is minimal in size, yielding minimal distortion when $\delta_\ell \leq \mu - r_e$. Thus, even from the perspective of diffraction considerations in the aberration-free case, the image point is quite accurately given by the pinhole model. As we depart from the focus reference plane, we find that the distortion magnitude becomes increasingly severe and unstable. For example, when $\mu^s_{\text{geo}} = 20$ μm, we find that on the interval $\delta_\ell \leq \mu - r_e$, it holds that $v_\ell < 5.4 \ll 20$ μm $= \mu^s$, while the mean and standard deviation of distortion magnitude for $\mu = 1.6 r_e$ increase to $\bar{v}_\ell = 3.7$ μm and $\sigma_{v_\ell} = 1.6$ μm, respectively. However, for the same absolute defocus at the sensor but of opposite sign, the defocus at the MLA may change substantially depending on the optical configuration. In this case, the defocus at the MLA is vastly greater at $\mu = 13.6 r_e$, with $v_\ell < 4.4$ μm, $\bar{v}_\ell = 2.6$ μm, and $\sigma_{v_\ell} = 0.9$ μm.

These statistics above are surprising, because they reveal the true complexity of radial distortion that is neither anticipated in the literature of plenoptic imaging nor predicted by geometrical optics. In fact, it was expected that whenever $\delta_\ell < \mu - r_e$, the distortion would be zero independent of the defocus value μ^s_{geo}. Remarkably, however, the distortion is of a measurable significance and becomes increasingly prominent for larger μ^s_{geo}. As the defocus increases, the asymmetric LF-PSF is larger in size, leading to a larger mean distortion magnitude. On the other hand, the fine structure of the fringe pattern in the intensity response continuously changes with δ_ℓ (and thus the radial position of the image point in the microimage), which leads to a larger overall fluctuation of the distortion; i.e., an increase in σ_{v_ℓ}.

Note that for microlenses of larger Fresnel numbers in which the Fresnel focal shift effect is negligible because most of the energy of the LF-PSF is encircled within the expected blur radius μ^s, the centroid of irradiance typically falls within this region for arbitrary defocus and vignetting. For the given setup, it was further discovered that for a vignetting of up to 84% of the maximum transmittable flux by the microlens, it constrains the distortion magnitude by the expected blur radius, (i.e., $v_\ell < \mu^s$). This is an elegant result because an immediate corollary of this inequality is that objects within the scene that are fully confined within the depth of field can only lead to subpixel distortions because $v_\ell < \mu^s \leq p$, where p is the pixel size. It also means that under such circumstances, the value of μ^s serves as a good upper bound to the distortion magnitude whenever most of the PSF's energy is locally confined to this region. One potential practical application of this result can be used as a constraint for rectification algorithms when correcting for radial distortions within the microimages. The distortion magnitude may exceed μ^s, but typically when the vignetting has become so severe that the normalised transmitted radiant flux through the microlens is close to 0 (e.g., $\mathscr{C}_o(\delta_\ell) < 0.2$).

6. CONCLUSION

In this paper, we use what we believe is a novel mathematical approach to present generalized semi-analytical expressions for the PSF of plenoptic cameras. As argued in [22], the unrestrictive range of defocus values permissible in the solution to the Debye diffraction integral provided by the ENZ theory also provide an appealing alternative to numerical Fourier transform methods when the defocused pupil functions require exceedingly large sampling densities. Adopting these results, the generalized semi-analytical equations ultimately allow accurate and efficient computational imaging for a general system, with arbitrary transmission functions and defocusing. By making less stringent assumptions to state-of-the-art methods, this diffraction model specifically provides a comparatively compact expression for the LF-PSF compared to those formerly proposed. The solution is perceptibly less complex and more extensive in applicability. The model's practical appeal can be found in the form of the solution in Eq. (33) that helps circumvent the iterative issue of numerical integration. This was procured by introducing an appropriate shifted coordinate frame to express the solution to the diffraction integral as a series of separable functions in which the Hankel transforms are solely of radial dependency. Consequently, this representation enhances the computational efficiency as the Hankel transforms have contours on circles in this shifted coordinate frame. An efficiency improved, yet approximating, solution to the LF-PSF was further derived in Appendix B given by Eq. (C6), which may be applied to render diffraction in novel architectures such as Fourier light field microscopy [4,5].

This model is also advantageous over former approaches heavily reliant on numerical methods, which are inefficient for computational imaging and potentially impractical for real-time image processing [21]. Additionally, each numerical integral will amplify residual errors in the overall calculation, but any subsequent analytical solutions to these diffraction integrals can help eradicate this problem for both higher accuracy and efficiency.

The derived series of Hankel transforms in the diffraction solution are rigorously proven to be convergent using bounds and the estimation lemma from complex analysis, as shown in Appendix A. In addition, in Section 4, the accuracy and legitimacy of the model is well verified against the gold standard Rayleigh–Sommerfeld diffraction integral, where high accuracy is demonstrated for even a few terms in the series expression of the LF-PSF.

In Section 3, for microlenses local to the optical axis of the main lens when paraxial imaging applies, a simple proof of the universal existence of diffractive mirror symmetries was also shown along axes intercepting the microimage centers. Image points at the same radial distance from the microimage centre only transform the LF-PSF by rotation, yielding isotropic radially distorted microimages. This is consistent with the LFC theorem as proven in [15]. The property is inevitable under the condition that the irradiance distribution incident on the MLA is radially symmetric and that the apertures are all circular. It is also self-evident from the solution that the diffractive response of the system is periodic between microimages of the same type. These results were easily shown because the formulation of the model explicitly reveals the underlying symmetries of the system's response in the mathematical form of its expression.

After establishing these general properties, it was additionally shown that one particular source of microimage radial distortion is vignetting, which we scrutinized in the diffraction limited plenoptic camera. To the best of our knowledge, this phenomena has not been previously studied. The analysis demonstrated the predicted distortions exceed those which would otherwise be estimated by a geometrical optics formalism, further justifying the necessity of an approach based on wave optics.

From where the encircled energy deteriorates about the ideal image point within the radius of the geometrical defocus in the sensor plane, the distortion diverges in severity toward the edge of the field of view of the microlens. By considering the mean and standard deviation, the severity and instability of these distortions were shown to increase with defocus at the sensor, even prior to when microlenses are subject to the edge effects of the main lens vignetting. Remarkably, distortions may be of measurable significance for an aberration-free system even for a perfectly focused image for which the geometric distortion is expected to be 0. Furthermore, for the setup considered, distortions were found to be typically bound by the expected blur radius defined by the maximum of the Airy disk radius and the radius of geometric defocus in the image plane. Thus, objects confined to the depth of field give rise to merely subpixel distortions. More counterintuitively, for equal and opposite geometrical defocus in the sensor plane, the distortions were found to be asymmetric. Although this can be well explained by the fact that imaging from depths that give equal absolute defocus at the sensor, often occur with a highly variable defocus at the MLA. More specifically, the distortion severity was found to be greater for lower image redundancy (i.e., for a smaller defocus of the main lens PSF at the MLA plane, in which a greater portion of the outer ring of the microimage suffers from vignetting).

Ultimately, radial distortions shear the epipolar geometry on the local scale of the microimages; therefore, a study of distortions to better comprehend and minimize the degradation they pose on the accuracy and resolution of depth maps is desirable. It is thus fitting that, in future work, quantification of the noise level in retrieved depth maps under different algorithms is made to comprehend the severity of these radial distortions on 3D scene reconstruction.

APPENDIX A: PROOF OF CONVERGENCE OF A SERIES FORMULA FOR THE LF-PSF

For the appendixes below, define $\| X\|_\infty = \sup\{|X(t)| : t \in T\}$ as the supremum norm assigned to real or complex-valued bounded functions X defined on a set T.

Lemma

(a) Given $z, w \in \mathbb{C}$, $|z+w| \le |z| + |w|$. (b) Any absolutely convergent series of complex numbers is convergent; that is, given $(c_j)_{j=0}^{\infty} \subset \mathbb{C} : \sum_{j=0}^{\infty} |c_j| < \infty \Rightarrow |\sum_{j=0}^{\infty} c_j| \le \sum_{j=0}^{\infty} |c_j| < \infty$.

Proposition

$\forall s \in \mathbb{N}, \exists M \in \mathbb{R} : |\mathcal{H}_s\{u_s(\rho); \gamma/C\}| \le \frac{M}{s!}\left(\frac{\gamma}{2}\right)^s$, for terms $u_s(\rho) = g_s(\rho) U(\rho) e^{i\alpha_{n_\ell}\rho^2}$, $\gamma = C\gamma_o$ and $C = r_e + \delta_\ell$.

Proof

Given the functions $g_s(\rho) = 2\bar{\phi}_{\delta_\ell}(\rho)\mathrm{sinc}(s\bar{\phi}_{\delta_\ell}(\rho))\chi_\Omega(\rho)$, $\forall s \in \mathbb{N}$, $\rho \in \mathbb{R}_+$ where $\Omega = [\max\{0, \delta_\ell - r_e\}, \delta_\ell + r_e)$, clearly $|g_0(\rho)| = 2|\bar{\phi}_{\delta_\ell}(\rho)|\chi_\Omega(\rho) \le 2\pi\chi_\Omega(\rho)$ as $|\bar{\phi}_{\delta_\ell}(\rho)| \le \pi$, while $|g_s(\rho)| \le \frac{2}{s}\chi_\Omega(\rho) \le 2\chi_\Omega(\rho), \forall s \in \mathbb{N}\backslash\{0\}, \rho \in \mathbb{R}_+$.

Therefore, we finally obtain $|g_s(\rho)| \le \max\{2\pi\chi_\Omega(\rho), 2\chi_\Omega(\rho)\}, \forall s \in \mathbb{N}, \rho \in \mathbb{R}_+$,

$$\Rightarrow |g_s(\rho)| \le 2\pi\chi_\Omega(\rho), \quad \forall s \in \mathbb{N}, \quad \rho \in \mathbb{R}_+. \tag{A1}$$

Next, from [30], holds $|J_s(z)| \le \left|\frac{z}{2}\right|^s \frac{e^{|\mathrm{Im}(z)|}}{\Gamma(s+1)}$, $s \ge -\frac{1}{2}$, where Γ is the gamma function and $\mathrm{Im}(z)$ is the imaginary part of z. Since the amplitude PSF of the main lens in the MLA plane $U(\rho)$ is continuous, on any closed interval it is then bounded so that $\|U\|_\infty < \infty$. It may be shown that a choice of $U(\rho) = \sqrt{\pi}\frac{\mathrm{NA}'}{\lambda}V_0^0(\rho)$ is bounded above.

There further holds $|e^{i\alpha_{n_\ell}\rho^2}| = 1$, for $\rho \in \mathbb{R}_+$. By definition of $u_s(\rho) = g_s(\rho)U(\rho)e^{i\alpha_{n_\ell}\rho^2}$, given $C = r_e + \delta_\ell$, we find

$$\begin{aligned}\therefore |u_s(\rho)J_s(\gamma_o\rho)\rho| &\le \frac{2\pi\rho\,\|U\|_\infty}{s!}\left(\frac{\gamma_o\rho}{2}\right)^s\chi_\Omega(\rho)\\ &\le \frac{2\pi C\,\|U\|_\infty}{s!}\left(\frac{C\gamma_o}{2}\right)^s\chi_\Omega(\rho),\end{aligned} \tag{A2}$$

$\forall s \in \mathbb{N}, \rho \in \mathbb{R}_+$.

One may write $\gamma_o(\varepsilon) = \frac{k}{b}\varepsilon$, where $0 \le \varepsilon < r_e + \bar{r}_\ell$ in restricting evaluation points to the microimage.

$\Rightarrow \|\gamma_o\|_\infty \le \frac{k}{b}(r_e + \bar{r}_\ell)$. Therefore, γ_o is bounded.

Therefore, since $u_s(\rho)J_s(\gamma_o\rho)\rho$ is a complex-valued continuous function that is clearly bounded on the contour $\mathbb{R}_+$ from Eq. (A2), then the estimation lemma holds; therefore, using the integral $\int_0^\infty \chi_\Omega(\rho)\mathrm{d}\rho = \int_{[\max\{0,\delta_\ell - r_e\},\delta_\ell + r_e)} \mathrm{d}\rho \le 2r_e$, where the constant $M = 4\pi C\,\|U\|_\infty r_e$,

$$\left|\int_0^\infty u_s(\rho)J_s(\gamma_o\rho)\rho\,\mathrm{d}\rho\right| \le \int_0^\infty |u_s(\rho)J_s(\gamma_o\rho)\rho|\,\mathrm{d}\rho, \tag{A3}$$

$$\Rightarrow |\mathcal{H}_s\{u_s(\rho); \gamma/C\}| \le \frac{M}{s!}\left(\frac{\gamma}{2}\right)^s, \tag{A4}$$

where $\gamma = C\gamma_o$.

Corollary

Let $S_N(\varepsilon, \psi) = \sum_{s=0}^{N-1} \epsilon_s i^s \cos(s\varphi(\psi))\mathcal{H}_s\{u_s(\rho); \gamma_o(\varepsilon)\}$. Then $S(\varepsilon, \psi) := \lim_{N\to\infty} S_N(\varepsilon, \psi) < \infty$ and an error estimate of the Nth partial sum of $S(\varepsilon, \psi)$ is given by the uniform bound $\|S - S_N\|_\infty \le \frac{2M(\|\gamma\|_\infty/2)^N}{N!} \min\left\{e^{\|\gamma\|_\infty/2}, \frac{1}{1-\|\gamma\|_\infty/2(N+1)}\right\}$, for $N > \|\gamma\|_\infty/2 - 1$, where the supremum norm $\|\cdot\|_\infty$ is considered on the set $D_\ell := [0, r_e + \delta_\ell) \times [0, 2\pi)$.

Proof

Let $u_s(\rho) = u_{0s}^0(\rho)$. Then, as $|\epsilon_s| \le 2$, $|i^s| \le 1$, $|\cos(s\varphi(\psi))| \le 1$, $\forall s \in \mathbb{N}$, $\psi \in [0, 2\pi)$ by the lemma and the proposition, $\forall N \in \mathbb{N}, (\varepsilon, \psi) \in D_\ell$,

$$
\begin{aligned}
|S_N(\varepsilon,\psi)| &\leq 2\sum_{s=0}^{N-1} |\mathcal{H}_s\{u_s(\rho);\gamma_o(\varepsilon)\}| \\
&\leq 2M\sum_{s=0}^{N-1}\frac{\left(\frac{\gamma(\varepsilon)}{2}\right)^s}{s!} < 2Me^{\gamma(\varepsilon)/2} < 2Me^{\|\gamma\|_\infty/2}, \\
&\Rightarrow \left|\sum_{s=0}^{\infty}\epsilon_s i^s\cos(s\varphi(\psi))\mathcal{H}_s\{u_s(\rho);\gamma_o(\varepsilon)\}\right| < \infty,
\end{aligned} \tag{A5}
$$

where the supremum norm $\|\gamma\|_\infty = \frac{kC}{b}(r_e+\bar{r}_\ell)$ is on the set D_ℓ with $C = r_e + \delta_\ell$.

The last two steps in the proof above follow because $\sum_{s=0}^{N}\left(\frac{\gamma(\varepsilon)}{2}\right)^s/s!$ is a bounded monotonically increasing sequence of partial sums, which converges to $e^{\|\gamma\|_\infty/2}$, so the partial sum $S_N(\varepsilon,\psi)$ must also converge as $N\to\infty$.

Now, consider the tail of the proven convergent series above, for which we find $\forall N\in\mathbb{N}$ and $(\varepsilon,\psi)\in D_\ell$,

$$
\begin{aligned}
|S(\varepsilon,\psi)-S_N(\varepsilon,\psi)| &\leq 2\sum_{s=N}^{\infty}|\mathcal{H}_s\{u_s(\rho);\gamma_o(\varepsilon)\}| \\
&\leq 2M\sum_{s=N}^{\infty}\frac{\left(\frac{\gamma(\varepsilon)}{2}\right)^s}{s!} \\
&\leq 2M\frac{\left(\frac{\gamma(\varepsilon)}{2}\right)^N}{N!}\left(\sum_{s=0}^{\infty}\frac{N\left(\frac{\gamma(\varepsilon)}{2}\right)^s}{\Pi_{k=0}^{s}(N+k)}\right) \\
&\leq 2M\frac{\left(\frac{\gamma(\varepsilon)}{2}\right)^N}{N!}\sum_{s=0}^{\infty}\frac{\left(\frac{\gamma(\varepsilon)}{2}\right)^s}{s!}
\end{aligned}
$$

$$
\Rightarrow |S(\varepsilon,\psi)-S_N(\varepsilon,\psi)| \leq 2M\frac{\left(\frac{\gamma(\varepsilon)}{2}\right)^N}{N!}e^{\gamma(\varepsilon)/2}, \tag{A6}
$$

having used the power series of the exponential function.

However, we also have for $N > \gamma(\varepsilon)/2 - 1$ and $(\varepsilon,\psi)\in D_\ell$,

$$
\begin{aligned}
|S(\varepsilon,\psi)-S_N(\varepsilon,\psi)| &\leq 2M\frac{\left(\frac{\gamma(\varepsilon)}{2}\right)^N}{N!}\left(\sum_{s=0}^{\infty}\frac{N\left(\frac{\gamma(\varepsilon)}{2}\right)^s}{\Pi_{k=0}^{s}(N+k)}\right) \\
&\leq 2M\frac{\left(\frac{\gamma(\varepsilon)}{2}\right)^N}{N!}\sum_{s=0}^{\infty}\left(\frac{\frac{\gamma(\varepsilon)}{2}}{N+1}\right)^s
\end{aligned}
$$

$$
\Rightarrow |S(\varepsilon,\psi)-S_N(\varepsilon,\psi)| = \frac{2M\left(\frac{\gamma(\varepsilon)}{2}\right)^N}{N!\left(1-\frac{\gamma(\varepsilon)}{2(N+1)}\right)}. \tag{A7}
$$

Since the inequalities above given by Eq. (A6) and Eq. (A7) hold for all $(\varepsilon,\psi)\in D_\ell$ and $N > \frac{\gamma(\varepsilon)}{2} - 1$, then we finally have the uniform error bound

$$
\|S - S_N\|_\infty \leq \frac{2M\left(\frac{\|\gamma\|_\infty}{2}\right)^N}{N!}\min\left\{e^{\frac{\|\gamma\|_\infty}{2}}, \frac{1}{1-\frac{\|\gamma\|_\infty}{2(N+1)}}\right\}, \tag{A8}
$$

for $N > \|\gamma\|_\infty/2 - 1$.

APPENDIX B: MICROLENS POWER TRANSMISSION

Consider an image that comes into focus at the sensor plane. Furthermore, in (ρ,ϕ) coordinates, consider a general distribution $\widetilde{U}(\rho,\phi)$ about $\widetilde{\boldsymbol{c}}_o$ in $\widetilde{\Pi}$ and let γ'_ℓ be the angle of the ray through the image point $\mathscr{P}'_o$ and the differential element in the microlens exit pupil with respect to the perpendicular to the sensor. From radiometry, the radiant flux transmitted through the microlens pupil defined by S_ℓ arriving at $\mathscr{P}'_o$, may be expressed as

$$
\Phi(\delta_\ell,\varphi_\ell) = \iint_{S_\ell}\cos^4(\gamma'_\ell)|\widetilde{U}(\rho,\phi)|^2\rho\,\mathrm{d}\rho\,\mathrm{d}\phi, \tag{B1}
$$

where $\widetilde{U}(\rho,\phi) = e^{-i\frac{kr_o}{z_o}\rho\cos(\phi-\theta_o)}U(\rho,\phi)$, relates the incident field of an extra-aerial source to that of an axial source.

If $b \gg r_e$ so that $\gamma'_\ell \approx \alpha'_\ell$ and the axial amplitude distribution U is circularly symmetric (i.e., $U(\rho,\phi) = U(\rho)$), then, by separation of variables, the flux is now $\Phi(\delta_\ell,\varphi_\ell) = \cos^4(\alpha'_\ell)\int_{\max(0,\delta_\ell - r_e/M_p)}^{\delta_\ell + r_e/M_p}|U(\rho)|^2\rho\left(\int_{\varphi_\ell-\bar{\phi}_{\delta_\ell}(\rho)}^{\varphi_\ell+\bar{\phi}_{\delta_\ell}(\rho)}\mathrm{d}\phi\right)\mathrm{d}\rho$, which upon integration over ϕ gives

$$
\Phi(\delta_\ell) = 2\cos^4(\alpha'_\ell)\int_{\max(0,\delta_\ell - r_e/M_p)}^{\delta_\ell + r_e/M_p}\bar{\phi}_{\delta_\ell}(\rho)|U(\rho)|^2\rho\,\mathrm{d}\rho, \tag{B2}
$$

because $\chi_{[a,b)}(\rho)$ represents the usual characteristic function.

The energy normalized aberration-free APSF is given by $U(\rho) = \sqrt{\pi}\frac{\mathrm{NA}'}{\lambda}V_0^0(\rho)$, where the radiant flux can be expressed as $\Phi(\delta_\ell) = 2\pi\cos^4(\alpha'_\ell)\left(\frac{\mathrm{NA}'}{\lambda}\right)^2\int_0^\infty\bar{\phi}_{\delta_\ell}(\rho)|V_0^0(\rho)|^2\rho\,\mathrm{d}\rho$.

Next, we define $\Phi_o = \max_{\delta_\ell\geq 0}\{\Phi(\delta_\ell)\}$ and consider the function $\mathscr{C}_o(\delta_\ell) = \Phi(\delta_\ell)/\Phi_o : [0,\infty)\to[0,1]$.

This is simply the fractional power transmitted through a microlens with respect to the maximum transmitted power.

To compare intensity distributions realistically across microlenses by considering the effects of main lens vignetting, define the pre-factor power transmission coefficient

$$
\mathscr{C}_{\delta_\ell} = \frac{\mathscr{C}_o(\delta_\ell)}{\int_0^{2\pi}\int_0^\infty I_\ell^s(r,\theta)r\,\mathrm{d}r\,\mathrm{d}\theta}. \tag{B3}
$$

APPENDIX C: ALTERNATIVE EXPRESSION FOR THE LF-PSF

The rate of convergence of the series expressions of the LF-PSF as given by Eqs. (26) and (33) decreases dramatically for $\delta_\ell \gg r_e$. Recall from Eq. (6) that the general expression for the amplitude distribution incident on the sensor plane in terms of the microimage coordinates $\boldsymbol{x}'_\ell$, can be expressed as

$$
U_\ell^s(\boldsymbol{x}'_\ell) = \iint_{\mathbb{R}^2} e^{i\alpha_{n_\ell}|\boldsymbol{x}|^2}U\left(\frac{\boldsymbol{x}-\boldsymbol{\delta}_\ell}{M_p}, a; p_o\right) P_{n_\ell}(\boldsymbol{x})e^{-i\frac{k}{b}\left[\boldsymbol{x}'_\ell - \frac{b\boldsymbol{\delta}_\ell}{M_p^2 a}\right]\cdot\boldsymbol{x}}\,\mathrm{d}^2\boldsymbol{x}. \tag{C1}
$$

When $\delta_\ell \gg r_e$, the curvature of the circular arc contours of the radial amplitude light distribution are sufficiently small in the microlens entrance pupil, so they may be approximated by linearization.

Next, define the rotated coordinate frame $\boldsymbol{x}'$ defined by the coordinate transformation $\boldsymbol{x} = \boldsymbol{R}(\varphi_\ell)\boldsymbol{x}'$, where the 2D rotation matrix

$$\boldsymbol{R}(\varphi_\ell) = \begin{pmatrix} \cos\varphi_\ell & -\sin\varphi_\ell \\ \sin\varphi_\ell & \cos\varphi_\ell \end{pmatrix}, \quad \text{(C2)}$$

rotates counterclockwise by φ_ℓ.

For a change of variables in the integration domain to the $\boldsymbol{x}'$ frame, and given that $|\boldsymbol{R}(\varphi_\ell)\boldsymbol{x}'| = |\boldsymbol{x}'|$, we obtain

$$\begin{aligned} U_\ell^s(\boldsymbol{x}'_\ell) &= \iint_{\mathbb{R}^2} e^{i\alpha_{n_\ell}|\boldsymbol{x}'|^2} U\left(\frac{\boldsymbol{R}(\varphi_\ell)\boldsymbol{x}' - \boldsymbol{\delta}_\ell}{M_p}, a;\ p_o\right) \\ &\quad P_{n_\ell}(\boldsymbol{R}(\varphi_\ell)\boldsymbol{x}') e^{-i\frac{k}{b}\left[\boldsymbol{x}'_\ell - \frac{b\boldsymbol{\delta}_\ell}{M_p^2 a}\right]\cdot\boldsymbol{R}(\varphi_\ell)\boldsymbol{x}'} \mathrm{d}^2\boldsymbol{x}' \\ &\approx \int_{-r_e}^{r_e} e^{i\alpha_{n_\ell}x'^2} U\left(\frac{\delta_\ell + x'}{M_p}\right) e^{i\frac{k}{b}\left(\boldsymbol{x}'_\ell\cdot\hat{\boldsymbol{\delta}}_\ell - \frac{b\delta_\ell}{M_p a}\right)x'} \\ &\quad \left(\int_{-\sqrt{r_e^2 - x'^2}}^{\sqrt{r_e^2 - x'^2}} e^{i\alpha_{n_\ell}y'^2} e^{-i\frac{k}{b}\boldsymbol{x}'_\ell\cdot\left(\boldsymbol{R}(-\frac{\pi}{2})\hat{\boldsymbol{\delta}}_\ell\right)y'} \mathrm{d}y'\right) \mathrm{d}x', \end{aligned} \quad \text{(C3)}$$

where the approximation follows for having assumed that the contours of the incident amplitude distribution are parallel to the y' axis. From geometry, a reasonable condition for the approximation's validity can be shown to obey $\delta_\ell[1 - \cos(\bar{\phi}_{\delta_\ell}(\delta_\ell))] \gg r_e$, which simplifies to $\delta_\ell \gg r_e$.

Equation (C3) above may be simplified further to give a more elegant result, in the special case $\alpha_{n_\ell} = 0$ (i.e. $b = f_{n_\ell}$).

As before, introducing the polar coordinates (r, θ), where $r = |\boldsymbol{x}'_\ell|$, $\theta = \arg\{\boldsymbol{x}'_\ell\}$, we find that $\boldsymbol{x}'_\ell \cdot \hat{\boldsymbol{\delta}}_\ell = -r\cos(\theta - \varphi_\ell)$ and $\boldsymbol{x}'_\ell \cdot (\boldsymbol{R}(-\frac{\pi}{2})\hat{\boldsymbol{\delta}}_\ell) = r\sin(\theta - \varphi_\ell)$. Allowing $x' = r_e\cos\tau$, upon substitution and integrating with respect to y' yields

$$\begin{aligned} U_\ell^s(r, \theta) &\approx -\frac{2r_e}{\frac{k}{b}r\sin(\theta - \varphi_\ell)} \int_0^\pi U\left(\frac{\delta_\ell + r_e\cos\tau}{M_p}\right) \\ &\quad e^{-i\frac{kr_e}{b}\left(r\cos(\theta-\varphi_\ell) + \frac{b\delta_\ell}{M_p a}\right)\cos\tau} \\ &\quad \sin\left(\frac{kr_e}{b}r\sin(\theta - \varphi_\ell)\sin\tau\right)\sin\tau\,\mathrm{d}\tau. \end{aligned} \quad \text{(C4)}$$

To determine the LF-PSF, we are now left to evaluate a single integral for each point in the sensor plane. It is thus preferable to extract the polar coordinates (r, θ) from the integrand.

By exploiting Euler's formula and successively applying the Jacobi–Anger expansion, we find that the product of terms

$$\begin{aligned} &e^{-i\frac{kr_e}{b}r\cos(\theta-\varphi_\ell)\cos\tau}\sin\left(\frac{kr_e}{b}r\sin(\theta - \varphi_\ell)\sin\tau\right) \\ &= 2i\sum_{s=1}^{\infty}(-i)^s\sin(s\tau)\sin(s(\theta - \varphi_\ell))J_s\left(\frac{kr_e r}{b}\right). \end{aligned} \quad \text{(C5)}$$

Substituting the expression above into Eq. (C4), and simplifying after applying term-by-term integration gives us the final result of the incident field distribution incident on the sensor plane. Taking the squared modulus and neglecting the constant pre-factor, we obtain

$$I_\ell^s(r, \theta) \approx \left|\sum_{s=1}^{\infty} a_s(\delta_\ell)\frac{\sin(s(\theta - \varphi_\ell))}{\sin(\theta - \varphi_\ell)}\frac{J_s(kr_e r/b)}{(kr_e r/b)}\right|^2, \quad \text{(C6)}$$

where the integral coefficients can be computed by the formula $a_s(\delta_\ell) = (-i)^s\int_0^\pi U\left(\frac{\delta_\ell + r_e\cos\tau}{M_p}\right)e^{-i\frac{k\delta_\ell r_e}{M_p a}\cos\tau}\sin\tau\,\sin(s\tau)\mathrm{d}\tau$. It is worth pointing out that the coefficients a_s are also in the form of a Fourier sine transform, as given by $\hat{f}^s(\nu) = \frac{1}{2\pi}\int_0^\infty f(\tau)\sin(\nu\tau)\mathrm{d}\tau$ of the complex function given by $f(\tau) = 2\pi(-i)^s U\left(\frac{\delta_\ell + r_e\cos\tau}{M_p}\right)e^{-i\frac{k\delta_\ell r_e}{M_p a}\cos\tau}\sin(\tau)\chi_{[0,\pi]}(\tau)$. The advantage of this form of the expression is that rather than having to iteratively compute for every (r, θ) coordinate the double integral in Eq. (C1), we may analytically calculate the intensity response everywhere in the microimage as an expansion series of Bessel functions of the first kind with a fixed set of integral coefficients $a_s(\delta_\ell)$.

Equation (C6) has immediate practical use for computational super-resolution in the novel FLFM with unprecedented resolution [4–6] where the defocus of the main lens PSF is large by comparison to the microlens aperture size and the MLA to sensor distance is set to the focal length of the microlens. It may be further proven that Eq. (C6) is also convergent, through a similar proof of the above proposition and corollary by simply using the additional bound $\left|\frac{\sin(s(\theta-\varphi_\ell))}{\sin(\theta-\varphi_\ell)}\right| \le s$, $\forall\theta \in [0, 2\pi)$, which follows from L'Hôpital's rule.

Acknowledgment. Author Mehdi Ardebili would like to give special thanks for the numerous conversations and unconditional support from my father Nader Ardebili.

Disclosures. The authors declare no conflicts of interest.

Data availability. Data underlying the results presented in this paper are not publicly available at this time but may be obtained from the authors upon reasonable request.

REFERENCES

1. A. Lumsdaine and T. Georgiev, "Full resolution lightfield rendering," Technical Report (Indiana University and Adobe Systems, 2008).
2. C. Perwass and L. Wietzke, "Single lens 3D-camera with extended depth-of-field," Proc. SPIE **8291**, 45–59 (2012).
3. H. Navarro, G. Saavedra, M. Martínez-Corral, M. Sjöström, and R. Olsson, "Depth-of-field enhancement in integral imaging by selective depth-deconvolution," J. Disp. Technol. **10**, 182–188 (2014).
4. G. Scrofani, J. Sola-Pikabea, A. Llavador, E. Sanchez-Ortiga, J. C. Barreiro, G. Saavedra, J. Garcia-Sucerquia, and M. Martínez-Corral, "FIMic: design for ultimate 3D-integral microscopy of in-vivo biological samples," Biomed. Opt. Express **9**, 335–346 (2018).
5. A. Llavador, J. Garcia-Sucerquia, E. Sánchez-Ortiga, G. Saavedra, and M. Martínez-Corral, "View images with unprecedented resolution in integral microscopy," OSA Contin. **1**, 40–47 (2018).
6. A. Stefanoiu, G. Scrofani, G. Saavedra, M. Martínez-Corral, and T. Lasser, "What about computational super-resolution in fluorescence Fourier light field microscopy?" Opt. Express **28**, 16554–16568 (2020).
7. R. Ng, "Fourier slice photography," ACM Trans. Graph. **24**, 735–744 (2005).

8. T. E. Bishop and P. Favaro, "The light field camera: extended depth of field, aliasing, and superresolution," IEEE Trans. Pattern Anal. Mach. Intell. **34**, 972–986 (2012).
9. R. Ng and P. M. Hanrahan, "Digital correction of lens aberrations in light field photography," in *International Optical Design, Technical Digest (CD)* (Optica Publishing Group, 2006), paper WB2.
10. T. Michels, A. Petersen, L. Palmieri, and R. Koch, "Simulation of plenoptic cameras," in *2018-3DTV-Conference: The True Vision-Capture, Transmission and Display of 3D Video (3DTV-CON)* (IEEE, 2018), pp. 1–4.
11. P. Mouroulis and J. Macdonald, *Geometrical Optics and Optical Design*, Oxford Series in Optical & Imaging Sciences (Oxford, 1997).
12. M. Broxton, L. Grosenick, S. Yang, N. Cohen, A. Andalman, K. Deisseroth, and M. Levoy, "Wave optics theory and 3D deconvolution for the light field microscope," Opt. Express **21**, 25418–25439 (2013).
13. J. W. Goodman, *Introduction to Fourier Optics* (Roberts and Company, 2005).
14. A. Grosso, K. Vonmetz, and T. Scharf, "Aberrations analysis of a focused plenoptic camera," Proc. SPIE **10677**, 585–594 (2018).
15. M. Ardebili and A. Erdmann, "Rectification algorithm of curvilinear epipolar geometry for scene depth retrieval in plenoptic imaging systems" (2013).
16. S. Li, Y. Zhu, C. Zhang, Y. Yuan, and H. Tan, "Rectification of images distorted by microlens array errors in plenoptic cameras," Sensors **18**, 2019 (2018).
17. M. Ardebili and A. Erdmann, "Point spread and illumination analysis of lightfield cameras," in *25th IEEE International Conference on Image Processing (ICIP)* (IEEE, 2018), pp. 659–663.
18. X. Jin, L. Liu, Y. Chen, and Q. Dai, "Point spread function and depth-invariant focal sweep point spread function for plenoptic camera 2.0," Opt. Express **25**, 9947–9962 (2017).
19. M. Levoy, R. Ng, A. Adams, M. Footer, and M. Horowitz, "Light field microscopy," ACM Trans. Graph. **25**, 924–934 (2006).
20. S. A. Shroff and K. Berkner, "High resolution image reconstruction for plenoptic imaging systems using system response," in *Imaging and Applied Optics Technical Papers, OSA Technical Digest (online)* (Optica Publishing Group, 2012), paper CM2B-2.
21. S. van Haver, "The extended Nijboer-Zernike diffraction theory and its applications, Ph.D. Thesis (Delft University of Technology, 2010).
22. A. Janssen, J. Braat, and P. Dirksen, "On the computation of the Nijboer-Zernike aberration integrals at arbitrary defocus," J. Mod. Opt. **51**, 687–703 (2004).
23. A. J. E. M. Janssen, "Extended Nijboer–Zernike approach for the computation of optical point-spread functions," J. Opt. Soc. Am. A **19**, 849–857 (2002).
24. J. Braat, P. Dirksen, and A. J. E. M. Janssen, "Assessment of an extended Nijboer–Zernike approach for the computation of optical point-spread functions," J. Opt. Soc. Am. A **19**, 858–870 (2002).
25. J. J. M. Braat, P. Dirksen, S. van Haver, and A. J. E. M. Janssen, "Detailed description of the ENZ approach," (2013), https://nijboerzernike.nl/_PDF/NijboerZernike_webpage_detailed_20151023.pdf.
26. M. Gu, *Advanced Optical Imaging Theory* (Springer, 2000), Vol.**75**.
27. E. W. Weisstein, "Circle-Circle Intersection," MathWorld–A Wolfram Web Resource (2018), https://mathworld.wolfram.com/Circle-CircleIntersection.html.
28. E. W. Weisstein, "Chebyshev Polynomial of the Second Kind," MathWorld–A Wolfram Web Resource (2018), https://mathworld.wolfram.com/ChebyshevPolynomialoftheSecondKind.html
29. S. R. Deans, *The Radon Transform and Some of Its Applications* (Courier Corporation, 2007).
30. M. Abramowitz and I. A. Stegun, eds. *Handbook of Mathematical Functions: with Formulas, Graphs, and Mathematical Tables* (Dover Publications, 1965).